

Physics and causally constrained discrete-time neural models of turbulent dynamical systems

Fabrizio Falasca* and Laure Zanna
Courant Institute School of Mathematics,
Computing and Data Science
New York University, New York, NY, USA

We present a framework for constructing physics and causally constrained neural models of turbulent dynamical systems from data. We first formulate a finite-time flow map with strict energy-preserving nonlinearities for stable modeling of temporally discrete trajectories. We then impose causal constraints to suppress spurious interactions across degrees of freedom. The resulting neural models accurately capture stationary statistics and responses to both small and large external forcings. We demonstrate the framework on the stochastic Charney–DeVore equations and on a symmetry-broken Lorenz–96 system. The framework is broadly applicable to reduced-order modeling of turbulent dynamical systems from observational data.

I. INTRODUCTION

Modeling and understanding complex turbulent dynamical systems often requires abandoning full microscopic descriptions in favor of reduced-order models, where coarse-grained variables evolve according to effective stochastic dynamics [1, 2]. Such reduced stochastic descriptions are fundamental across physics, ranging from chemical physics [3, 4], neuroscience [5, 6], mathematical physics [7, 8], turbulence [9–11], climate science [12–18], and many others. In practice, one is often faced with an inverse problem: given long trajectories of a Markovian, coarse-grained system, construct a data-driven model that faithfully reproduces its statistical and dynamical features [11, 19–31]. Recent advances in machine learning further contribute to inverse modeling by providing flexible neural network architectures for data-driven emulation, with promising applications in fluid dynamics [32–34], weather [35, 36], and climate science [37–41]. However, neural network-based models are typically agnostic to the underlying physics. This can lead to several failure modes, including long-term nonphysical behavior, such as violations of energy conservation [22, 24, 42] and consequent blow-up of solutions [43], and incorrect responses to external forcings [44–46]. The latter limitation is particularly critical for scientific applications, where models are used for process understanding and exploration of “*what if?*” scenarios. Crucially, a model’s ability to respond to forcings is inherently linked to causality, since cause–effect relationships in physical systems are defined by their response to external interventions [47–50], typically realized via perturbation–response experiments [51, 52]. In this Letter, we address these challenges by presenting an efficient strategy to construct physics and causally constrained neural models of turbulent dynamical systems from data alone. We focus on the less explored context of discrete-time

modeling, which avoids inconsistencies arising in applications when continuous-time conservation principles are applied to temporally coarse-grained data. Given a trajectory $\mathbf{x}_t = (x_t^{(1)}, x_t^{(2)}, \dots, x_t^{(n)})$ of a multivariate discrete Markovian system, our framework proceeds in two steps: (i) *Physics Constraints*: We propose a neural model, with strict energy-conserving nonlinearities, tailored to realistic, discrete-time coarse-grained observations. (ii) *Causal Constraints*: We identify direct causal couplings $x^{(j)} \rightarrow x^{(k)}$ from data via the Fluctuation-Dissipation Theorem (FDT) and use this information to suppress spurious, non-causal interactions during model training. The FDT plays a fundamental role here, as it provides a rigorous bridge between forced and natural fluctuations [53–55], allowing for a causal inference strategy in the interventional sense directly from unperturbed, stationary data [31, 56, 57]. Ultimately, the physics constraints, specifically formulated for discrete settings, provide the foundation of our approach. These physical priors promote robust inference in data-scarce regimes and ensure long-term numerical stability. Furthermore, this structural rigidity naturally bounds the impact of imperfect causal estimates: even if the inferred causal links contain errors, the resulting model remains confined to a physically consistent solution. As a representative application, we consider climate dynamics, where accurate prediction of forced responses is essential [31]. We test the framework on two benchmarks: a stochastic version of the Charney–DeVore model [58] and a symmetry-broken Lorenz–96 system [59] as a higher-dimensional testbed. The resulting neural emulators are stable, capture stationary statistics, and reproduce responses to both weak and strong external forcings, including time-dependent shifts of the attractor, despite being trained exclusively on unperturbed data.

* fabri.falasca@nyu.edu

II. FRAMEWORK: PHYSICS AND CAUSAL CONSTRAINTS

A. Finite-time flow map with energy-preserving nonlinearities

Previous work. We build on the abstract representation of turbulent dynamical systems often adopted by Majda and collaborators [2, 54] $\dot{\mathbf{x}} = \mathbf{F} + \mathbf{A}\mathbf{x} + \mathbf{B}(\mathbf{x}, \mathbf{x}) + \Sigma\xi(t)$, which arises when a large class of fluid flows are projected onto orthogonal basis functions. The quadratic term is energy-conserving, satisfying $\mathbf{x} \cdot \mathbf{B}(\mathbf{x}, \mathbf{x}) = 0$ [60, 61], with the system’s energy defined as $E = (1/2)\mathbf{x}^T\mathbf{x}$. \mathbf{F} represents external forcing, and the linear operator \mathbf{A} is typically decomposed as $\mathbf{A} = \mathbf{L} + \mathbf{D}$, where \mathbf{L} (skew-symmetric) and \mathbf{D} (symmetric, negative-definite) represent dispersion and dissipation, respectively. $\Sigma\xi(t)$ is a stochastic forcing, with $\xi(t)$ denoting a standard Gaussian white-noise process. Following recent work on neural closure and modeling [10, 28, 62, 63], we replace $\mathbf{B}(\mathbf{x}, \mathbf{x})$ by a general nonlinear operator $\mathbf{S}(\mathbf{x})\mathbf{x}$, where $\mathbf{S}(\mathbf{x})$ is constrained to be skew-symmetric, $\mathbf{S}^T(\mathbf{x}) = -\mathbf{S}(\mathbf{x})$. This preserves the key physical property $\mathbf{x}^T\mathbf{S}(\mathbf{x})\mathbf{x} = 0$, so the nonlinear term redistributes energy across modes without net injection or dissipation. The importance of energy-conserving nonlinearities in data-driven models of turbulent systems was highlighted in [22]. Details are presented in the Supplemental Material (SM) Sec. I.

Finite-time flow map formulation. Observational data are fundamentally discrete and temporally coarse-grained, yet physics constraints are typically defined strictly in the continuous limit. To resolve this discrepancy, we introduce a discrete, abstract formulation of turbulent dynamical systems with exact energy-conserving nonlinearities for arbitrary time increments:

$$\mathbf{x}_{t+1} = \mathbf{f}(\mathbf{x}_t) = \mathbf{F} + \mathbf{M}\mathbf{Q}(\mathbf{x}_t)\mathbf{x}_t + \Sigma\xi_t, \quad (1)$$

where \mathbf{F} and $\Sigma\xi_t$ represent the effective deterministic and stochastic forcings integrated over the finite time step. The nonlinear operator $\mathbf{Q}(\mathbf{x}_t)$ is constrained to be strictly orthogonal ($\mathbf{Q}^T\mathbf{Q} = \mathbf{I}$). Thus, the deterministic map splits into an energy-preserving rotation, $\mathbf{v}_t = \mathbf{Q}(\mathbf{x}_t)\mathbf{x}_t$, followed by a linear transformation $\mathbf{M}\mathbf{v}_t$. The isolated nonlinear term contributes no net growth or decay to the energy budget, strictly preserving the L_2 -norm of the state:

$$\|\mathbf{Q}(\mathbf{x}_t)\mathbf{x}_t\|^2 = \mathbf{x}_t^T \mathbf{Q}^T(\mathbf{x}_t)\mathbf{Q}(\mathbf{x}_t)\mathbf{x}_t = \|\mathbf{x}_t\|^2.$$

Consequently, energy growth in the forward map is bounded by the dominant singular value of \mathbf{M} . While additional constraints on \mathbf{M} could be imposed, they are often not required in practice and may degrade performance. In the SM (Sec. II), we provide mathematical justification for Eq. (1). First, we demonstrate that in the continuous limit this mapping arises as a Lie–Trotter

splitting scheme [64], and we further derive the corresponding effective deterministic and stochastic forcings \mathbf{F} and $\Sigma\xi_t$. As illustrative examples, we recast the deterministic Lorenz-63 system and a stochastic triad model within this framework. Second, we return to the data-driven setting and show that the proposed discrete formulation in Eq. (1) enables stable learning from severely sub-sampled data, where both numerical integrators and continuous-time data-driven models fail.

Neural model fitting. Given a stationary trajectory \mathbf{x}_t , we parametrize the deterministic drift $\mathbf{f}(\mathbf{x}_t)$ by training a multilayer perceptron (MLP) to minimize the mean squared error $\text{MSE}(\mathbf{x}_{t+1}, \mathbf{f}(\mathbf{x}_t))$. States are standardized to zero mean and unit variance. We enforce the orthogonality of $\mathbf{Q}(\mathbf{x}_t)$ by predicting the matrix exponential $\mathbf{Q}(\mathbf{x}_t) = \exp(\mathbf{S}(\mathbf{x}_t))$ of a skew-symmetric matrix $\mathbf{S}(\mathbf{x}_t)$. Crucially, the linear terms are initialized with a “first guess” ordinary least squares (OLS) solution, while the MLP is initialized to yield $\mathbf{Q}(\mathbf{x}_t) = \mathbf{I}$. This ensures the joint optimization starts from a Linear Inverse Model (LIM) [19] baseline before learning the nonlinear corrections. Here, the diffusion matrix Σ is estimated as a diagonal matrix from the standard deviation of the deterministic residuals; the general framework captures spatial correlations via the Cholesky decomposition of the residual covariance. Further implementation details, including careful data rescaling, are discussed in SM Sec. I.

B. Fluctuation–Dissipation Theorem (FDT) and causality

Given an n -dimensional stochastic nonlinear system $\mathbf{x}_t = (x_t^{(1)}, x_t^{(2)}, \dots, x_t^{(n)})$, the FDT [54, 65] states that the linear response, in the ensemble average sense, of a degree of freedom $x_t^{(k)}$ to an infinitesimally small impulse perturbation $\delta x_0^{(j)}$ applied to component $x_0^{(j)}$ can be written as:

$$R_t^{k,j} = \frac{\delta \langle x_t^{(k)} \rangle}{\delta x_0^{(j)}} = -\langle x_t^{(k)} s_j(\mathbf{x}_0) \rangle, \quad (2)$$

$$s(\mathbf{x}) = \nabla \log \rho(\mathbf{x}).$$

$\rho(\mathbf{x})$ is the system’s invariant density and $s(\mathbf{x})$ is the *score function* of the system [66, 67]. The brackets $\langle \cdot \rangle$ represents ensemble averages, computed over the invariant density. Eq. (2) provides a rigorous strategy for inferring causal relations in physical systems in the interventional sense from data alone [31, 56]. Values at the shortest time scale $R_1^{k,j}$ encode direct causal links $x^{(j)} \rightarrow x^{(k)}$ and are used to construct our causal constraints. Evaluating Eq. (2) requires the score function $s(\mathbf{x})$. We leverage recent advances in score-based generative modeling [43, 68–73] to learn $s(\mathbf{x})$ directly from data for use in the analytical FDT formula [66, 67], therefore bypassing traditional quasi-Gaussian approximations [54, 74]. Specifically, we employ the exact score-matching estimator [75] to evaluate the score directly on the system’s

attractor. The resulting estimate is further refined using the correction procedure of [66] (see SM Sec. III for details).

Causal constraints. Given a discrete stochastic systems $x_{t+1}^{(i)} = f_i(x_t^{(1)}, x_t^{(2)}, \dots, x_t^{(n)}) + \sigma_i \xi_t^{(i)}$ with $i = 1, 2, \dots, n$, a perturbation to $x^{(j)}$ can affect $x^{(k)}$ at the next time step only if f_k depends on $x^{(j)}$. Thus, $\partial f_k / \partial x^{(j)} \equiv 0$ implies the *absence* of a direct causal link and consequently, a vanishing short-time response $R_1^{k,j} = 0$. In practice, the system’s Jacobian is not observable from data, and a reliable numerical estimation is unfeasible in high-dimensional systems. However, the short-time response $R_1^{k,j}$ can be efficiently estimated from unperturbed data using the FDT in Eq. (2). A vanishing response at the shortest resolved time scale thus implies $\langle \partial f_k(\mathbf{x}) / \partial x^{(j)} \rangle = 0$ for $j \neq k$. This information is used to constrain neural architectures. Thus, given a long trajectory of $\mathbf{x}(t)$, we first estimate the short-time response operator $\mathbf{R}_{t=1} \in \mathbb{R}^{n,n}$. We then construct a binary adjacency matrix $\mathbf{A} \in \mathbb{R}^{n,n}$, by thresholding \mathbf{R}_1 . $A^{k,j} = 0$ denoting the absence of a direct causal link $x^{(j)} \rightarrow x^{(k)}$, and $A^{k,j} = 1$ denoting its presence. A visual inspection of $R_1^{k,j}$ on a logarithmic scale often reveals a clear separation between significant links and noise. The absence of such separation suggests a densely connected system with no need for causal constraints. To provide an unsupervised criterion, we propose the following procedure:

- i. *Self-interactions.* We assume that for any dissipative dynamical system $x^{(j)} \rightarrow x^{(k)}$ and therefore $A^{j,j} = 1$.
- ii. *Cross-interactions.* We consider the off-diagonal values of $R_1^{k,j}$, $j \neq k$, and apply a logarithmic transformation $\ln |R_1^{k,j}|$, separating potential causal links (larger responses) from the bulk of spurious, near-zero interactions. A k-means algorithm [76] ($k=2$) is used to partition these values into two clusters. An entry of $A^{k,j} = 1$ is set if its corresponding $\ln |R_1^{k,j}|$ value belongs to the cluster with the larger centroid; otherwise, it is set to 0 (absence of causal link $x^{(j)} \rightarrow x^{(k)}$).

The matrix $A^{k,j}$ is then used to constrain neural emulators. Specifically, the MSE minimization is regularized with a causal penalty:

$$\begin{aligned} \mathcal{L} &= \mathcal{L}_{\text{MSE}} + \mathcal{L}_{\text{Causal}} \\ &= \text{MSE}(\mathbf{x}_{t+1}, \mathbf{f}(\mathbf{x}_t)) + \lambda \sum_{k,j \in \mathcal{S}} \left(\frac{\partial f_k}{\partial x^{(j)}} \right)^2, \end{aligned} \quad (3)$$

where \mathcal{S} is the set of pairs (k, j) for which $A_{k,j} = 0$. λ is a parameter determining the strength of the regularization.

Imperfect causal estimates. False negatives in the adjacency matrix $A^{k,j}$ (true links penalized as noncausal) can degrade the learned emulator when learning via Eq. (3). Physics-constrained architectures mitigates the impact of imperfect causal estimates through rigid structural priors. Additionally, if false negatives are suspected, via validation with stationary and perturbed

statistics (see paragraph below), a more robust penalty can be employed:

$$\mathcal{L}_{\text{Causal}}^{\text{Robust}} = \lambda \sum_{k,j \in \mathcal{S}} \min \left(\left(\frac{\partial f_k}{\partial x^{(j)}} \right)^2, \gamma \right), \quad (4)$$

which bounds the penalty once $(\partial f_k / \partial x^{(j)})^2 \geq \gamma$, allowing the MSE term to dominate when interactions are mistakenly excluded. An heuristic estimate for γ based on the FDT operator $R_1^{k,j}$ is given in Sec. IC in the SM.

Possible limitations for idealized systems. Causal constraints rely on zeros of the ensemble-averaged Jacobian to restrict the state-dependent Jacobian. In idealized systems with *exact* symmetries (e.g., the Lorenz ’63 system [60]), nonzero local couplings may cancel in the average, yielding $\langle \partial f_k(\mathbf{x}) / \partial x^{(j)} \rangle = 0$ even when $\partial f_k / \partial x^{(j)} \neq 0$. Such cases require a symmetry-reduction step [77, 78]. However, this is rarely restrictive for realistic, partially observed turbulent flows (e.g., weather and climate), which lack exact symmetries and admit multiple coarse-grained representations, see Sec. IV in the SM for details.

Assessing causal constraints. Unlike rigid physical priors, the utility of causal regularization is system-dependent and contingent on the accuracy of the data-driven causal discovery. The benefit of augmenting physics-constrained models with causal information can be assessed directly from data by comparing the FDT-based operator (Eq. (2)) with the emulators’ response operators (SM Sec. V). When the inferred causal structure is informative, the resulting emulator improves linear response predictions without degrading stationary statistics.

III. PHYSICS AND CAUSAL CONSTRAINTS IN PRACTICE

We first illustrate the proposed framework on a six-dimensional stochastic system, highlighting the causal inference procedure and the benefits of the imposed constraints. We then focus on a symmetry-broken Lorenz–96 system as a more demanding test case, evaluating both its response to strong external forcings and robustness against imperfect causal estimates.

A. Stochastic Charney-DeVore model

We consider a stochastic version of the Charney–DeVore model [58], “CdV” hereafter, later reformulated by De Swart [79]. The model was obtained as a six-dimensional Galerkin truncation of the barotropic vorticity equation on a β -plane channel with topography. The model has been studied in the context of large-scale atmospheric circulation [80–83] and takes the following

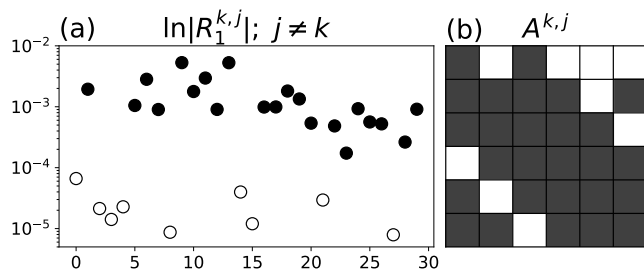


FIG. 1: Causal constraining of the CdV model (Eq. (5)) from data using the FDT and score matching. Panel (a): The 30 off-diagonal responses $\ln|R_1^{k,j}|$, flattened and plotted against a dummy index. Causal links are identified via k-means clustering ($k = 2$), shown as filled and open circles. Panel (b): Resulting causal adjacency matrix $A^{k,j}$: $A^{k,j} = 1$ (dark) for responses in the cluster with the larger centroid, and $A^{k,j} = 0$ (white) otherwise. Example: the first row $A^{1,j}$ implies $x_{t+1}^{(1)} = f_1(x_t^{(1)}, x_t^{(3)})$.

form:

$$\begin{aligned}
 \dot{x}_1 &= \tilde{\gamma}_1 x_3 - C(x_1 - x_1^*) + \sigma \xi_1(t), \\
 \dot{x}_2 &= -(\alpha_1 x_1 - \beta_1) x_3 - C x_2 - \delta_1 x_4 x_6 + \sigma \xi_2(t), \\
 \dot{x}_3 &= (\alpha_1 x_1 - \beta_1) x_2 - \gamma_1 x_1 - C x_3 + \delta_1 x_4 x_5 + \sigma \xi_3(t), \\
 \dot{x}_4 &= \tilde{\gamma}_2 x_6 - C(x_4 - x_4^*) + \varepsilon(x_2 x_6 - x_3 x_5) + \sigma \xi_4(t), \\
 \dot{x}_5 &= -(\alpha_2 x_1 - \beta_2) x_6 - C x_5 - \delta_2 x_4 x_3 + \sigma \xi_5(t), \\
 \dot{x}_6 &= (\alpha_2 x_1 - \beta_2) x_5 - \gamma_2 x_4 - C x_6 + \delta_2 x_4 x_2 + \sigma \xi_6(t).
 \end{aligned} \tag{5}$$

We integrate Eq. (5) with a RK4 scheme for $T = 10^7$ time-steps at $dt = 0.01$, i.e. 10^5 Model Time Units (MTU). The resulting 6-dimensional trajectory is then treated as a discrete time series $\mathbf{x}_t = (x_t^{(1)}, \dots, x_t^{(6)})$ from which we want to learn the discrete flow map in Eq. (1). The parameters and their physical interpretation are reported in Sec. V of the SM. This stochastic model features fast decay of autocorrelations and regular, unimodal probability distributions: such properties are relevant for coarse-grained climate dynamics as found both in models and observations [84–87], and underlie the reduced-order modeling of realistic, turbulent systems [2]. The main text highlights the identification of the causal Adjacency matrix and response to weak and strong forcing of variable x_1 ; a comprehensive analysis is provided in the SM.

a. Causal Adjacency matrix from data. Given a trajectory of the CdV model, we infer the direct causal links. The strategy is summarized in Figure 1. We infer the response operator at the shortest time scale $R_1^{k,j} = -\langle x_1^{(k)} s_j(\mathbf{x}_0) \rangle$, apply the transformation $\ln|R_1^{k,j}|$ and split the large responses from the spurious non-causal ones via k-means clustering ($k=2$); see Figure 1(a). This information is used to define the Adjacency matrix in Figure 1(b).

b. Neural emulators. We learn two discrete physics-constrained neural models, with and without causal constraints, from the long trajectory \mathbf{x}_t . We denote these models as “Physics” and “Physics & Causal” emulators.

c. Stationary statistics. We simulate a long trajectory of $T = 10^7$ time steps with the neural models. We examine two stationary statistics: the invariant distribution (PDF) and the autocorrelation functions (ACFs). Both emulators faithfully reproduce these stationary statistics; see Sec. VII of the SM.

d. Perturbed statistics: linear regime. We analyze the impulse response operator for the ensemble mean and variance. A small impulse perturbation $\delta x_0^{(j)}$ is applied at $t = 0$, and the response of observables $A(x_t^{(k)}) = x_t^{(k)}$ (mean) and $A(x_t^{(k)}) = (x_t^{(k)} - \mu_t^{(k)})^2$ (variance) is measured, μ_t representing the time-dependent mean (see SM Sec. VI). As a representative example, we perturb $x_0^{(6)}$ and report the self-response of $x_t^{(1)}$ in mean and variance (Fig. 2(a,c)). Both emulators reproduce the response operator well, with the causally constrained model outperforming the non-causal one. This improvement is robust, as shown in SM Sec. VIII, where we report the time-dependent MSE of the responses $R_t^{k,j}$ aggregated over all pairs j, k . By contrast, we also trained a vanilla MLP network (no physics and no causal constraints). The vanilla model reproduced well the stationary distribution of the system, but suffered instability even under small perturbations (not shown).

e. Perturbed statistics: nonlinear regime. We probe the nonlinear response by applying a large step forcing \mathbf{F} to both the numerical model and the neural emulators. As in the linear analysis, the forcing acts on $x^{(6)}$, $\mathbf{F} = (0, 0, 0, 0, 0, \sigma_6)$ for $t \geq 0$, where σ_6 is the standard deviation of $x^{(6)}$. We simulate an ensemble of 10^5 realizations and measure the response of the ensemble mean and variance relative to the unperturbed stationary distribution. Results are shown in Figure 2(b,d). The numerical model exhibits a pronounced transient before relaxing to a new equilibrium after ~ 40 model time units, reflecting a shift of the attractor in state space. Both emulators remain stable under this strong forcing and predict the response well. The physics- and causally-constrained model generally outperforms the physics-only emulator. This improvement is robust as shown in Sec. IX where we report the time-dependent MSE of the responses aggregated over all perturbation experiments.

IV. SYMMETRY-BROKEN LORENZ-96 SYSTEM

We define a symmetry-broken version of the Lorenz-96 (L96) [59] system as

$$\dot{x}_j = (x_{j+1} - x_{j-2})x_{j-1} - x_j + F_j + \sigma \xi_j(t), \tag{6}$$

with $j = 1, \dots, J$ and periodic boundary conditions $x_j = x_{j+J}$. We set $J = 20$. The time-independent forc-

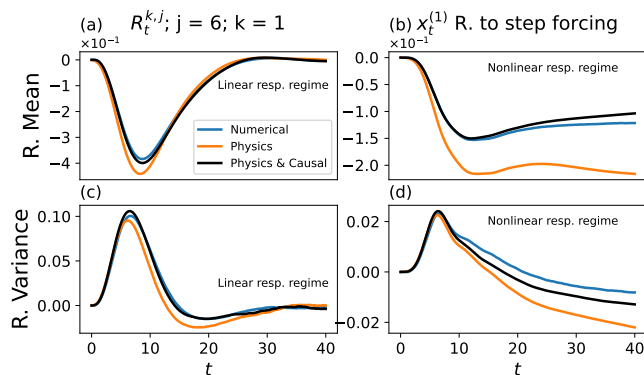


FIG. 2: Perturbed statistics. Panel (a) and (c): linear response regime. Panel (a): Time-dependent, response in ensemble mean of variable $x_t^{(1)}$ to an impulse perturbation $\delta x_0^{(6)}$ imposed on $x_0^{(6)}$ at time $t = 0$. Formally: $R_t^{1,6} = \delta \langle x_t^{(1)} \rangle / \delta x_0^{(6)}$. Panel (c): same as Panel (a) but for response in ensemble variance. Panel (b) and (d): nonlinear response regime. Panel (b): Time-dependent response of the ensemble mean of $x^{(3)}$ to a step function forcing. Forcing: step function $\mathbf{F} = (0, 0, 0, 0, 0, \sigma_6)$ for $t \geq 0$, applied on the right-hand side of the numerical model and emulators. σ_6 is the standard deviation of $x^{(6)}$. Panel (d): same as Panel (b) but for the ensemble variance. Notably, an unconstrained vanilla MLP reproduces stationary statistics well but becomes unstable even under small perturbations (not shown).

ing is defined as $F_j = F + \eta_j$, where $\eta_j \sim \mathcal{N}(0, \sigma_F^2)$ with $\sigma_F = 10$. Because the forcing includes a random component, we impose a minimum value of 4 to maintain positivity. This site-dependent forcing (ranging from 4 to ~ 31) breaks translational invariance and induces spatially heterogeneous turbulence. Physically, the localized forcing can be interpreted as topographic effects. The stochastic term $\sigma \xi_j(t)$, with $\sigma = 5$, represents unresolved fast processes. The system in Eq. (6) serves as a prototype of a turbulent dynamical system, with strong mixing, exponential decay of autocorrelations, many unstable directions, and regular distributions even in the deterministic limit [2, 9]. For reproducibility, the specific F_j values are reported in SM Sec. X. We simulate a long trajectory of $T = 10^6$ time steps with $dt = 0.01$ (10^4 model time units). The 20-dimensional trajectory is treated as a discrete time series $\mathbf{x}_t = (x_t^{(1)}, \dots, x_t^{(20)})$ from which we want to learn the discrete flow map in Eq. (1). We infer the causal adjacency matrix following the protocol described in the previous Sections. As shown in Fig. 3, the framework largely recovers the correct causal structure, including the periodic boundary conditions, despite the turbulent nonlinear dynamics. Two false negatives and one false positive are identified (red and blue in Fig. 3). Because the inferred causal structure is imperfect, causal constraints are imposed through the robust

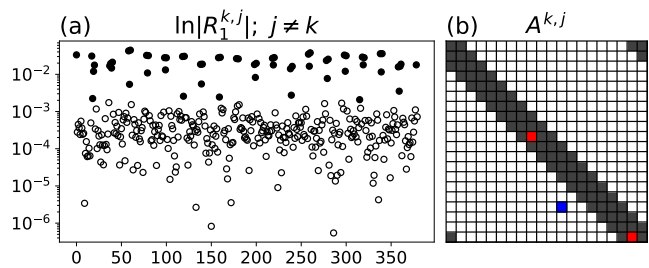


FIG. 3: Same as Figure 1, but for the L96 system defined in Eq. (6). Red squares indicate false negatives: true physical links erroneously labeled as noncausal. The blue square indicates a false positive: a spurious link erroneously labeled as causal. Example: the first row $A^{1,j}$ indicates a functional dependency

$$\mathbf{x}_{t+1}^{(1)} = f_1(x_t^{(19)}, x_t^{(20)}, x_t^{(1)}, x_t^{(2)})$$

loss in Eq. (4). We then train a “Physics” and a “Physics & Causal” constrained neural emulators. Both reproduce the invariant density and autocorrelation functions (SM Sec. XA) and accurately capture the linear responses (not shown). Here we probe the nonlinear response regime by applying a Gaussian forcing centered at lattice site $j = 10$,

$$G_j = w \exp\left(-\frac{d(j, \mu)^2}{2\ell^2}\right), \quad (7)$$

$$d(j, \mu) = \min(|j - \mu|, J - |j - \mu|),$$

with $\mu = 10$ and $\ell = 3$. The distance function $d(j, \mu)$ is needed to account for the periodic boundary conditions. The forcing amplitude is determined by computing the total standard deviation σ_{Tot} (which is on the order of the individual standard deviation σ_j at each site $x^{(j)}$) and setting $w = 10\sigma_{\text{Tot}}$. This constitutes a severe perturbation, an order of magnitude larger than the natural variability of any single degree of freedom. As depicted in Fig. 4(top-left and bottom-left panels), this strong forcing significantly shifts the mean and variance of the attractor. The purely physics-constrained emulator already captures these statistical changes accurately. Augmenting the model with causal constraints yields a slightly improved representation of the response, particularly in the variance. Importantly, we emphasize that given the robust causal penalty in Eq. (4), the causal model maintains this high performance even if the imposed causal priors are imperfect. Finally, we also trained a vanilla MLP without physical or causal constraints: the unconstrained network was more difficult to train, requiring ~ 10 times more epochs to achieve a comparable loss. Although this baseline model reproduced the stationary distribution well and remained stable under the large forcing in Eq. (7) (not shown), it exhibited very large errors in the predicted response as also reported in Figure Fig. 4.

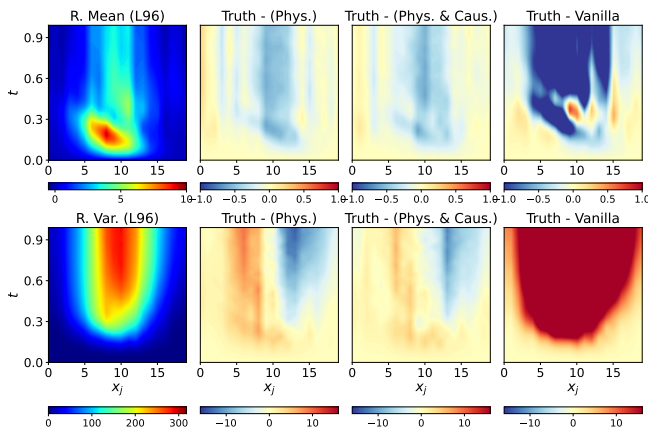


FIG. 4: Response of the L96 system to a large Gaussian forcing [Eq. (7)] applied and held constant for $t \geq 0$.

Top row: ensemble-mean response. Bottom row: ensemble-variance response. Left: ground truth. Second column: difference between the physics-constrained emulator and the truth. Third column: difference between the physics- and causally constrained emulator and the truth. Fourth column: difference between a completely unconstrained (no physics and no causal constraints) model and the truth.

V. DISCUSSION AND CONCLUSIONS

We have proposed a framework for physics and causally constrained reduced-order neural modeling of turbulent dynamical systems. The physics-constrained neural models are here formulated as discrete finite-time maps with strictly energy-conserving nonlinearities. This generalizes continuous-time conservation laws into a formulation inherently amenable to coarse-grained, discrete observational data. Building upon this architectural foundation, we demonstrated how causal information, derived via the fluctuation-dissipation theorem (FDT), can be practically enforced to suppress spurious functional dependen-

cies within the neural model. Conservation laws alone do not uniquely determine the system’s dynamics; causal information provides additional constraints on admissible interactions. Crucially, while the energy-conserving architecture is prescribed *a priori* as a geometric prior, causal constraints must be inferred from data, requiring careful handling of estimation uncertainty. The resulting constrained models yield stable emulators that accurately capture stationary statistics and responses to both weak and strong external forcings, despite being trained exclusively on unforced data. A central challenge for practical data-driven applications remains the construction of a Markovian coarse-grained representation from high-dimensional spatiotemporal data, as emphasized in classical theory [88] and explored in recent work [31, 50, 89]. However, given an approximate Markovian, coarse-grained representation of a spatiotemporal system, informed by physics and domain knowledge, the proposed constrained discrete neural models can be readily adopted. A natural extension of this work is its application to observational climate data to construct reduced-order emulators of the global atmosphere and ocean. More broadly, while our test cases are motivated by climate dynamics, this methodology provides a practical strategy for neural modeling of general complex turbulent systems in reduced coordinate spaces.

Code availability Codes will be soon available at <https://github.com/FabriFalasca/Physics-and-causally-constrained-neural-models/>

ACKNOWLEDGMENTS

This research was supported by Schmidt Sciences, LLC, through the M²LInES project. Computational resources and support were provided in part by the NYU IT High Performance Computing facilities, services, and staff. F.F. is grateful to Rory Basinski, Matthieu Blanke and Andre Souza for enriching discussions on this subject.

-
- [1] P. Castiglione, M. Falcioni, A. Lesne, and A. Vulpiani, *Chaos and Coarse Graining in Statistical Mechanics* (Cambridge University Press, 2008).
 - [2] A. Majda, *Introduction to Turbulent Dynamical Systems in Complex Systems* (Springer Cham, 2016).
 - [3] S. Izvekov and G. Voth, Multiscale coarse graining of liquid-state systems, *J. Chem. Phys* **123**, <https://doi.org/10.1063/1.2038787> (2005).
 - [4] J.-H. Prinz, H. Wu, M. Sarich, B. Keller, M. Senne, M. Held, J. Chodera, C. Schütte, and F. Noé, Markov models of molecular kinetics: Generation and validation, *J. Chem. Phys* **134**, <https://doi.org/10.1063/1.3565032> (2011).
 - [5] L. Harrison, O. David, and K. Friston, Stochastic models of neuronal dynamics, *Phil. Trans. R. Soc. B* **360**, 1075–1091 (2005).
 - [6] A. Rangan, L. Tao, G. Kovacic, and D. Cai, Multiscale modeling of the primary visual cortex, *IEEE Eng Med Biol Mag.* **28**, 19 (2009).
 - [7] A. Roberts, Normal form transforms separate slow and fast modes in stochastic dynamical systems, *Physica A: Statistical Mechanics and its Applications* **387**, 12 (2008).
 - [8] A. J. Roberts, Resolving the multitude of microscale interactions accurately models stochastic partial differential equations, *LMS Journal of Computation and Mathematics* **9**, 193–221 (2006).
 - [9] A. Majda and D. Qi, Strategies for Reduced-Order Models for Predicting the Statistical Responses and Uncertainty Quantification in Complex Turbulent Dynamical Systems, *SIAM REVIEW* **60**, <https://doi.org/10.1137/16M1104664> (2018).

- [10] B. Sanderse, Non-linearly stable reduced-order models for incompressible flow with energy-conserving finite volume methods, *Journal of Computational Physics* **421**, 109736 (2020).
- [11] N. Chen and H. Liu, Minimum reduced-order models via causal inference, *Nonlinear Dyn* **113**, 11327–11351 (2025).
- [12] K. Hasselmann, Stochastic climate models part i. theory., *Tellus* **28**, 473 (1976).
- [13] A. J. Majda, I. Timofeyev, and Vanden-Eijnden, Models for stochastic climate prediction, *Proc. Natl. Acad. Sci. USA* **96**, 14687–14691 (1999).
- [14] A. Majda, C. Franzke, and D. Crommelin, Normal forms for reduced stochastic climate models, *Proc. Natl. Acad. Sci.* **10**, 3649–3653 (2010).
- [15] M. Ghil and V. Lucarini, The physics of climate variability and climate change, *Rev. Mod. Phys.* **92**, 035002 (2020).
- [16] V. Lucarini and M. Chekroun, Theoretical tools for understanding the climate crisis from Hasselmann’s programme and beyond, *Nat Rev Phys* (2023) (2023).
- [17] V. Kitsios, L. Cordier, and T. J. O’Kane, Three-dimensional proper orthogonal decomposition reduced-order model of the global atmospheric climate, *International Journal of Heat and Fluid Flow* **119**, 110253 (2026).
- [18] V. Kitsios, L. Cordier, and T. J. O’Kane, Proper orthogonal decomposition reduced-order model of the global oceans, *Theor. Comput. Fluid Dyn.* **38**, 707–727 (2024).
- [19] C. Penland, Random Forcing and Forecasting Using Principal Oscillation Pattern Analysis, *Monthly Weather Review* **117**, 2165 (1989).
- [20] I. Horenko, Finite element approach to clustering of multidimensional time series, *SIAM J. Sci. Comp.* **32**, 68–83 (2010).
- [21] G. Pavliotis and A. Stuart, Parameter estimation for multiscale diffusions, *J. Stat. Phys.* **127**, 741–781 (2007).
- [22] A. Majda and J. Harlim, Physics constrained nonlinear regression models for time series, *NONLINEARITY* **26**, 201–217 (2013).
- [23] S. Kravtsov, D. Kondrashov, and M. Ghil, Multilevel Regression Modeling of Nonlinear Processes: Derivation and Applications to Climatic Variability, *Journal of Climate* **18**, 4404–4424 (2005).
- [24] D. Kondrashov, M. Chekroun, and M. Ghil, Data-driven non-markovian closure models, *Physica D: Nonlinear Phenomena* **297**, 33 (2015).
- [25] J. L. Callahan, J.-C. Loiseau, G. Rigas, and S. L. Brunton, Nonlinear stochastic modelling with langevin regression, *Proceedings of the Royal Society A: Mathematical, Physical and Engineering Sciences* **477**, 20210092 (2021), <https://royalsocietypublishing.org/rspa/article-pdf/doi/10.1098/rspa.2021.0092/725688/rspa.2021.0092.pdf>.
- [26] A. Souza, Representing turbulent statistics with partitions of state space. part 1. theory and methodology., *J. Fluid Mech.* **997** (2024).
- [27] N. Chen and A. J. Majda, Conditional gaussian systems for multiscale nonlinear stochastic systems: Prediction, state estimation and uncertainty quantification, *Entropy* **20**, 10.3390/e20070509 (2018).
- [28] L. Giorgini, Score-Based Modeling of Effective Langevin Dynamics, *Arxiv* <https://doi.org/10.48550/arXiv.2505.01895> (2025).
- [29] R. Azencott, A. Beri, and I. Timofeyev, Adaptive subsampling for parametric estimation of gaussian diffusions, *J Stat Phys* **139**, 1066–1089 (2010).
- [30] F. Ferretti, V. Chardès, T. Mora, A. M. Walczak, and I. Giardina, Building general langevin models from discrete datasets, *Phys. Rev. X* **10**, 031018 (2020).
- [31] F. Falasca, Probing forced responses and causality in data-driven climate emulators: Conceptual limitations and the role of reduced-order models, *Phys. Rev. Res.* **7**, 043314 (2025).
- [32] N. Geneva and N. Zabarav, Modeling the dynamics of pde systems with physics-constrained deep auto-regressive networks, *Journal of Computational Physics* **403**, 109056 (2020).
- [33] M. Milano and P. Koumoutsakos, Neural network modeling for near wall turbulent flow, *Journal of Computational Physics* **182**, 1 (2002).
- [34] P. Vlachas, G. Arampatzis, C. Uhler, and et al., Multiscale simulations of complex systems by learning their effective dynamics, *Nat Mach Intell* **4**, 359–366 (2022).
- [35] J. Pathak, S. Subramanian, P. Harrington, S. Raja, A. Chattopadhyay, M. Mardani, T. Kurth, D. Hall, Z. Li, K. Aizzadenesheli, P. Hassanzadeh, K. Kashinath, and A. Anandkumar, FourCastNet: A Global Data-driven High-resolution Weather Model using Adaptive Fourier Neural Operators, *arXiv e-prints*, arXiv:2202.11214 (2022), arXiv:2202.11214 [physics.ao-ph].
- [36] B. Bonev and et al., FourCastNet 3: A geometric approach to probabilistic machine-learning weather forecasting at scale, *arXiv e-prints* 10.48550/arXiv.2507.12144 (2025).
- [37] O. Watt-Meyer, G. Dresdner, J. McGibbon, S. K. Clark, B. Henn, J. Duncan, N. D. Brenowitz, K. Kashinath, M. S. Pritchard, B. Bonev, M. E. Peters, and C. S. Bretherton, ACE: A fast, skillful learned global atmospheric model for climate prediction, *arXiv e-prints*, arXiv:2310.02074 (2023), arXiv:2310.02074 [physics.ao-ph].
- [38] O. Watt-Meyer, B. Henn, J. McGibbon, S. K. Clark, A. Kwa, W. A. Perkins, and C. S. Bretherton, ACE2: Accurately learning subseasonal to decadal atmospheric variability and forced responses, *arXiv e-prints* <https://arxiv.org/abs/2411.11268> (2024).
- [39] H. Guan, T. Arcomano, A. Chattopadhyay, and R. Maulik, LUCIE: A Lightweight Uncoupled Climate Emulator with long-term stability and physical consistency for O(1000)-member ensembles, *arXiv* <https://doi.org/10.48550/arXiv.2405.16297> (2025).
- [40] W. Chapman, J. Schreck, Y. Sha, D. Gagne II, D. Kimpara, L. Zanna, K. Mayer, and J. Berner, CAMulator: Fast Emulation of the Community Atmosphere Model, *Arxiv* <https://doi.org/10.48550/arXiv.2504.06007> (2025).
- [41] S. Dheeshjith, A. Subel, A. Adcroft, J. Busecke, C. Fernandez-Granda, S. Gupta, and L. Zanna, Samudra: An AI global ocean emulator for climate., *Geophysical Research Letters* **52**, e2024GL114318 (2025).
- [42] N. Mücke and B. Sanderse, Physics-aware generative models for turbulent fluid flows through energy-consistent stochastic interpolants, *Arxiv* <https://doi.org/10.48550/arXiv.2504.05852> (2025).
- [43] C. Pedersen, L. Zanna, and J. Bruna, Thermalizer: Stable autoregressive neural emulation of spatiotemporal chaos, *Arxiv* <https://doi.org/10.48550/arXiv.2503.18731>

- (2025).
- [44] X. Tian, D. Holdaway, and D. Kleist, Evaluating machine learning weather models for data assimilation: Fundamental limitations in tangent linear and adjoint properties, *Geophysical Research Letters* **53**, e2025GL119402 (2026).
- [45] S. Van Loon, M. Rugenstein, and E. A. Barnes, Reanalysis-based Global Radiative Response to Sea Surface Temperature Patterns: Evaluating the Ai2 Climate Emulator, *Geophysical Research Letters* **52**, e2025GL115432 (2025).
- [46] B. Zhang and T. Merlis, The Equilibrium Response of Atmospheric Machine-Learning Models to Uniform Sea Surface Temperature Warming, *Arxiv* <https://doi.org/10.48550/arXiv.2510.02415> (2026).
- [47] J. Ismael, Reflections on the asymmetry of causation, *Interface Focus* **12**, 20220081 (2023).
- [48] E. Aurell and G. Del Ferraro, Causal analysis, correlation- response, and dynamic cavity, *J. of Phys.: Conference Series* **699**, 012002 (2016).
- [49] V. Lucarini, Revising and Extending the Linear Response Theory for Statistical Mechanical Systems: Evaluating Observables as Predictors and Predictands, *J Stat Phys* **173**, 1698–1721 (2018).
- [50] D. Lucente, M. Baldovin, F. Cecconi, M. Cencini, N. Cociagli, A. Puglisi, M. Viale, and A. Vulpiani, Conceptual and practical approaches for investigating irreversible processes, *New Journal of Physics* **27**, 041201 (2025).
- [51] T. Paus, Inferring causality in brain images: a perturbation approach, *Philos Trans R Soc Lond B Biol Sci.* **29**, 041201 (2005).
- [52] J. Bloch-Johnson, M. A. A. Rugenstein, M. J. Alessi, C. Proistosescu, M. Zhao, B. Zhang, A. I. L. Williams, J. M. Gregory, J. Cole, Y. Dong, M. L. Duffy, S. M. Kang, and C. Zhou, The green’s function model intercomparison project (gfmip) protocol, *Journal of Advances in Modeling Earth Systems* **16**, e2023MS003700 (2024).
- [53] R. H. Kraichnan, Classical fluctuation-relaxation theorem, *Phys. Rev.* **113**, 1181 (1959).
- [54] A. J. Majda, R. V. Abramov, and M. J. Grote, *Information Theory and Stochastics for Multiscale Nonlinear Systems* (CRM Monograph Series, American Mathematical Society, 2005).
- [55] V. Lucarini, M. S. Gutiérrez, J. Moroney, and N. Zagli, A general framework for linking free and forced fluctuations via koopmanism, *Chaos, Solitons & Fractals* **202**, 117540 (2026).
- [56] M. Baldovin, F. Cecconi, and A. Vulpiani, Understanding causation via correlations and linear response theory, *Physical Review Research* **2**, 043436 (2020).
- [57] F. Cecconi, G. Costantini, C. Guardiani, M. Baldovin, and A. Vulpiani, Correlation, response and entropy approaches to allosteric behaviors: a critical comparison on the ubiquitin case, *Physical Biology* **20**, 056002 (2023).
- [58] J. Charney and J. DeVore, Multiple flow equilibria in the atmosphere and blocking, *Journal of the atmospheric sciences* **36**, 1205 (1979).
- [59] E. Lorenz, Predictability: a problem partly solved, *Seminar on Predictability*, 4-8 September 1995 **1**, 1 (1995).
- [60] E. Lorenz, Deterministic nonperiodic flow, *J. Atmospheric Sci.* **20**, 130–141 (1963).
- [61] F. Kwasiok, Reduced atmospheric models using dynamically motivated basis functions, *Journal of the Atmospheric Sciences* **64**, 3452–3474 (2007).
- [62] T. van Gastelen, W. Edeling, and B. Sanderse, Energy-conserving neural network for turbulence closure modeling, *Journal of Computational Physics* **508**, 113003 (2024).
- [63] F. Roth, D. Klein, M. Kannapinn, J. Peters, and O. Weeger, Stable Port-Hamiltonian Neural Networks, *Arxiv* <https://doi.org/10.48550/arXiv.2502.02480> (2025).
- [64] N. Bou-Rabee and H. Owhadi, Long-run accuracy of variational integrators in the stochastic context, *SIAM Journal on Numerical Analysis* **48**, 278 (2010), <https://doi.org/10.1137/090758842>.
- [65] U. Marconi, A. Puglisi, L. Rondoni, and A. Vulpiani, Fluctuation-dissipation: Response theory in statistical physics, *Phys. Rep.* **461** (2008).
- [66] L. T. Giorgini, K. Deck, T. Bischoff, and A. Souza, Response theory via generative score modeling, *Phys. Rev. Lett.* **133**, 267302 (2024).
- [67] L. Giorgini, F. Falasca, and A. Souza, Predicting Forced Responses of Probability Distributions via the Fluctuation-Dissipation Theorem and Generative Modeling, *Arxiv* <https://doi.org/10.48550/arXiv.2504.13333> (2025).
- [68] Y. Song, J. Sohl-Dickstein, D. P. Kingma, A. Kumar, S. Ermon, and B. Poole, Score-based generative modeling through stochastic differential equations, *arXiv preprint arXiv:2011.13456* <https://doi.org/10.48550/arXiv.2011.13456> (2021).
- [69] Y. Song, S. Garg, J. Shi, and S. Ermon, Sliced score matching: A scalable approach to density and score estimation, *arXiv preprint arXiv:1905.07088* <https://doi.org/10.48550/arXiv.1905.07088> (2021).
- [70] A. Souza, S. Silvestri, K. Deck, T. Bischoff, R. Ferrari, and G. Flierl, Surface to seafloor: A generative ai framework for decoding the ocean interior state, *arXiv preprint* <https://doi.org/10.48550/arXiv.2504.15308> (2025).
- [71] I. Price, A. Sanchez-Gonzalez, F. Alet, and et al., Probabilistic weather forecasting with machine learning, *Nature* **637**, 84–90 (2025).
- [72] N. Brenowitz and et al., Climate in a bottle: Towards a generative foundation model for the kilometer-scale global atmosphere, *arXiv preprint arXiv:2505.06474* <https://doi.org/10.48550/arXiv.2505.06474> (2025).
- [73] A. Lobbe, D. Crisan, and O. Lang, Bayesian inference for geophysical fluid dynamics using generative models, *Philosophical Transactions of the Royal Society A: Mathematical, Physical and Engineering Sciences* **383**, 20240321 (2025), <https://royalsocietypublishing.org/rsta/article-pdf/doi/10.1098/rsta.2024.0321/2819094/rsta.2024.0321.pdf>.
- [74] C. E. Leith, Climate response and fluctuation dissipation, *Journal of The Atmospheric Science* **32**, 2022–2026 (1975).
- [75] A. Hyvärinen, Estimation of non-normalized statistical models by score matching, *Journal of Machine Learning Research* **6**, 695–709 (2005).
- [76] F. Pedregosa, G. Varoquaux, A. Gramfort, V. Michel, B. Thirion, O. Grisel, M. Blondel, P. Prettenhofer, R. Weiss, V. Dubourg, J. Vanderplas, A. Passos, D. Cournapeau, M. Brucher, M. Perrot, and E. Duchesnay, Scikit-learn: Machine learning in Python, *Journal of Machine Learning Research* **12**, 2825 (2011).
- [77] P. Cvitanović, R. Artuso, R. Mainieri, G. Tanner, and G. Vattay, *Chaos: Classical and Quan-*

- tum* (ChaosBook.org, Niels Bohr Institute, Copenhagen, 2016).
- [78] R. Miranda and E. Stone, The proto-lorenz system, *Physics Letters A* **178**, 105 (1993).
- [79] H. De Swart, Low-order spectral models of the atmospheric circulation: A survey, *Acta Applicandae Mathematica* **11**, 49 (1988).
- [80] D. Crommelin and A. Majda, Strategies for Model Reduction: Comparing Different Optimal Bases, *Journal of the Atmospheric Sciences* **61**, 2206–2217 (2004).
- [81] D. T. Crommelin, J. Opsteegh, and F. Verhulst, A mechanism for atmospheric regime behavior, *Journal of the atmospheric sciences* **61**, 1406 (2004).
- [82] J. Dorrington and T. Palmer, On the interaction of stochastic forcing and regime dynamics, *Nonlinear Processes in Geophysics* **30**, 49 (2023).
- [83] T. Grafke and E. Vanden-Eijnden, Numerical computation of rare events via large deviation theory, *Chaos: An Interdisciplinary Journal of Nonlinear Science* **29** (2019).
- [84] C. Franzke and A. Majda, Low-order stochastic mode reduction for a prototype atmospheric GCM, *Journal of the Atmospheric Sciences* **2**, 457–479 (2006).
- [85] J. Berner and G. Branstator, Linear and nonlinear signatures in the planetary wave dynamics of an agcm: Probability density functions, *Journal of the Atmospheric Sciences* **64**, 117–136 (2007).
- [86] P. Sura, M. Newman, C. Penland, and P. Sardeshmukh, Multiplicative noise and non-Gaussianity: A paradigm for atmospheric regimes?, *Journal of Climate* **62**, 1391–1409 (2005).
- [87] A. Majda, R. Abramov, and B. Gershgorin, High skill in low-frequency climate response through fluctuation dissipation theorems despite structural instability, *Proc. Natl. Acad. Sci.* **107**, 581–586 (2010).
- [88] L. Onsager and S. Machlup, Fluctuations and irreversible processes, *Phys. Rev.* **91**, 1505 (1953).
- [89] A. J. Majda and B. Gershgorin, Link between statistical equilibrium fidelity and forecasting skill for complex systems with model error, *Proceedings of the National Academy of Sciences* **108**, 12599 (2011), <https://www.pnas.org/doi/pdf/10.1073/pnas.1108132108>.
- [90] A. J. Majda and Y. Yuan, Fundamental limitations of ad hoc linear and quadratic multi-level regression models for physical systems, *Discrete and Continuous Dynamical Systems - Series B* **17**, 10.3934/dcdsb.2012.17.1333 (2012).
- [91] A. Paszke and et al., PyTorch: An Imperative Style, High-Performance Deep Learning Library, Arxiv <https://doi.org/10.48550/arXiv.1912.01703> (2025).
- [92] Z. Tian and C. Gu, A numerical algorithm for lyapunov equations, *Applied Mathematics and Computation* **202**, 44 (2008).
- [93] M. Falcioni, S. Isola, and A. Vulpiani, Correlation functions and relaxation properties in chaotic dynamics and statistical mechanics, *Physics Letters A* **144**, 341 (1990).
- [94] A. Gritsun and G. Branstator, Climate response using a three-dimensional operator based on the fluctuation–dissipation theorem, *Journal of The Atmospheric Science* , 2558–2575 (2007).
- [95] A. Majda, B. Gershgorin, and Y. Yuan, Low-Frequency Climate Response and Fluctuation–Dissipation Theorems: Theory and Practice , *Journal of the Atmospheric Sciences* **67**, 1186–1201 (2010).
- [96] M. Hutchinson, A stochastic estimator of the trace of the influence matrix for laplacian smoothing splines, *Communications in Statistics-Simulation and Computation* **18**, 1059–1076 (1989).
- [97] F. Falasca, P. Perezhogin, and L. Zanna, Data-driven dimensionality reduction and causal inference for spatiotemporal climate fields, *Phys. Rev. E* **109**, 044202 (2024).

Supplemental Material for:
Physics and causally constrained discrete-time neural models
of turbulent dynamical systems

Fabrizio Falasca and Laure Zanna
 Courant Institute School of Mathematics, Computing and Data Science, New York University

(Dated: April 14, 2026)

I. PHYSICS AND CAUSALLY CONSTRAINED MODELS

A. Previous work on continuous models

The models considered in this work build on the following abstract representation of turbulent dynamical systems:

$$\dot{\mathbf{x}} = \mathbf{F} + \mathbf{A}\mathbf{x} + \mathbf{B}(\mathbf{x}, \mathbf{x}) + \Sigma\xi(t). \quad (1)$$

Such a functional form, characterized by energy-conserving quadratic nonlinearities $\mathbf{B}(\mathbf{x}, \mathbf{x})$, typically arises when turbulent dynamical systems are projected onto a reduced orthogonal basis [54, 60]. Here \mathbf{F} represents an external forcing, \mathbf{A} a linear operator, and $\Sigma\xi(t)$ a stochastic forcing parametrizing unresolved degrees of freedom. Majda and collaborators [22, 90] first emphasized the importance of constraining nonlinear regression models inferred from time series so that the nonlinear terms are energy conserving. A practical data-driven implementation of such constraints was later proposed by Kondrashov et al. [24]. While most work has focused on constraining the nonlinear component $\mathbf{B}(\mathbf{x}, \mathbf{x})$, the linear operator can also be physically constrained. Indeed, many physical systems of the form in Eq. (1) admit a decomposition of the linear operator \mathbf{A} into dispersive and dissipative components, $\mathbf{A} = \mathbf{L} + \mathbf{D}$, where \mathbf{L} is skew-symmetric ($\mathbf{L}^T = -\mathbf{L}$, representing dispersion) and \mathbf{D} is symmetric negative-definite ($\mathbf{D}^T = \mathbf{D} < 0$), representing dissipation [2, 9]. Recent work by Sandefer and collaborators [10, 62] has further highlighted a more general representation of nonlinear interactions using skew-symmetric operators of the form $\mathbf{S}(\mathbf{x})\mathbf{x}$. This motivates a more general formulation:

$$\dot{\mathbf{x}} = \mathbf{F} + \mathbf{A}\mathbf{x} + \mathbf{S}(\mathbf{x})\mathbf{x} + \Sigma(\mathbf{x})\xi(t), \quad (2)$$

where the linear operators \mathbf{L} and \mathbf{D} satisfy the constraints described above, and the nonlinear operator is required to be skew-symmetric, $\mathbf{S}(\mathbf{x})^T = -\mathbf{S}(\mathbf{x})$. Additionally, we impose $\mathbf{S}(0) = 0$, ensuring that $\mathbf{S}(\mathbf{x})$ contains only nonlinear contributions.

Energy conservation of the skew-symmetric nonlinear operator $\mathbf{S}(\mathbf{x})$. For completeness, we show how the skew-symmetric nonlinear operator leads to energy conservation. We define the system “energy” as the quadratic functional

$$E = (1/2)\mathbf{x}^T\mathbf{x},$$

whose time derivative is

$$\frac{dE}{dt} = \frac{d}{dt}\left(\frac{1}{2}\mathbf{x}^T\mathbf{x}\right) = \mathbf{x}^T\frac{d\mathbf{x}}{dt}.$$

Isolating the nonlinear contribution in Eq. (2),

$$\frac{dE}{dt} = \mathbf{x}^T\mathbf{S}(\mathbf{x})\mathbf{x}.$$

Since $\mathbf{S}(\mathbf{x})$ is skew-symmetric, $\mathbf{S}(\mathbf{x})^T = -\mathbf{S}(\mathbf{x})$, it follows that

$$\mathbf{x}^T\mathbf{S}(\mathbf{x})\mathbf{x} = 0,$$

leading to energy conservation $dE/dt = 0$ of the nonlinear terms. We emphasize that this conservation property applies only to the nonlinear term.

B. Proposed discrete-time models

The structural constraints discussed above are formally derived for continuous-time dynamical systems in the limit $dt \rightarrow 0$. However, neural emulators are often inferred from discrete time series. In practice, given T observations $\mathbf{x}_1, \mathbf{x}_2, \dots, \mathbf{x}_T$ sampled at a fixed interval, this effective time step reflects (non-unique) choices of temporal coarse-graining rather than a mere numerical discretization parameter [31]. It is therefore desirable to design a model trained as a discrete-time predictor $\mathbf{x}_{t+1} \approx \mathbf{f}(\mathbf{x}_t)$, while still preserving the fundamental symmetries showcased above.

In particular, we focus on the crucial constraint of energy conservation within the nonlinear term. In the discrete case, we require that the nonlinear update conserves the L_2 norm of the state it acts on; i.e., the ‘‘energy’’ of the system at time t is defined as $\|\mathbf{x}_t\|^2$. As introduced in the main text, we propose the following functional form:

$$\begin{aligned} \mathbf{v}_t &= \mathbf{Q}(\mathbf{x}_t)\mathbf{x}_t, \\ \mathbf{x}_{t+1} &= \mathbf{F} + \mathbf{M}\mathbf{v}_t + \Sigma\xi_t, \end{aligned} \quad (3)$$

where \mathbf{F} and $\Sigma\xi_t$ represent the effective deterministic and stochastic forcings, arising from integrating over the discrete finite time step (not to be confused with their continuous counterparts in Eq. (2)).

The nonlinear operator $\mathbf{Q}(\mathbf{x}_t)$ is constrained to be strictly orthogonal ($\mathbf{Q}^\top \mathbf{Q} = \mathbf{I}$). The isolated nonlinear term $\mathbf{v}_t = \mathbf{Q}(\mathbf{x}_t)\mathbf{x}_t$ contributes no net growth or decay to the energy budget, strictly preserving the L_2 -norm of the state:

$$\|\mathbf{v}_t\|^2 = \|\mathbf{Q}(\mathbf{x}_t)\mathbf{x}_t\|^2 = \mathbf{x}_t^\top \mathbf{Q}^\top(\mathbf{x}_t)\mathbf{Q}(\mathbf{x}_t)\mathbf{x}_t = \mathbf{x}_t^\top \mathbf{I}\mathbf{x}_t = \|\mathbf{x}_t\|^2.$$

Geometrically, the full deterministic update rule acts as two sequential operations: a rotation in state space, $\mathbf{v}_t = \mathbf{Q}(\mathbf{x}_t)\mathbf{x}_t$, followed by a linear transformation $\mathbf{M}\mathbf{v}_t$. The overall energy growth or decay of the system is exclusively controlled by the singular values of the linear operator \mathbf{M} . Additional constraints can, in principle, be applied to guarantee global dissipative properties by strictly bounding the maximum singular value of \mathbf{M} . We view these strict constraints on the linear operator \mathbf{M} as optional, and potentially reducing the flexibility of the resulting data-driven model. We therefore leave potential constraints on \mathbf{M} to future work.

1. Details on the emulator implementation

Given a n -dimensional discrete dynamical system encoded in as a long trajectory $\mathbf{x} \in \mathbb{R}^{n,T}$, with length T , we aim in fitting as:

$$\mathbf{x}_{t+1} = \mathbf{f}(\mathbf{x}_t) + \Sigma\xi_t \quad (4)$$

where the deterministic drift is

$$\mathbf{f}(\mathbf{x}_t) = \mathbf{F} + \mathbf{M}\mathbf{S}(\mathbf{x}_t)\mathbf{x}_t.$$

a. Fitting the deterministic drift $\mathbf{f}(\mathbf{x}_t)$. We fit the deterministic dynamics such that $\mathbf{x}_{t+1} \approx \mathbf{f}(\mathbf{x}_t)$. We do so by minimizing the mean squared error (MSE) over the trajectory:

$$\mathcal{L} = \text{MSE}(\mathbf{x}_{t+1}, \mathbf{f}(\mathbf{x}_t)). \quad (5)$$

- All terms comprising the discrete map, $\mathbf{f}(\mathbf{x}_t) = \mathbf{F} + \mathbf{M}\mathbf{Q}(\mathbf{x}_t)\mathbf{x}_t$, are trained jointly via gradient descent. The primary challenge in this joint optimization is the initialization step. To resolve this, the linear components \mathbf{F} and \mathbf{M} are first pre-computed using Ordinary Least Squares (OLS) to capture the baseline linear dynamics. This deterministic ‘‘first guess’’ serves as the initialization for the network parameters.
- The nonlinear operator $\mathbf{Q}(\cdot)$ is parameterized by a Multi-Layer Perceptron (MLP) with a SiLU activation function. To strictly enforce orthogonality ($\mathbf{Q}^\top \mathbf{Q} = \mathbf{I}$) across all forward passes, we employ the following architectural construction:

- The MLP maps a state $\mathbf{x}_t \in \mathbb{R}^n$ to $n(n-1)/2$ independent scalar values.

- These values populate the upper-triangular elements of a matrix, which is then used to construct an exact skew-symmetric matrix $\mathbf{S}(\mathbf{x}_t) = -\mathbf{S}^\top(\mathbf{x}_t)$.
- We map the skew-symmetric $\mathbf{S}(\mathbf{x}_t)$ to an orthogonal operator via the matrix exponential, $\mathbf{Q}(\mathbf{x}_t) = \exp(\mathbf{S}(\mathbf{x}_t))$, or the computationally efficient Cayley transform, $\mathbf{Q}(\mathbf{x}_t) = (\mathbf{I} - \mathbf{S}(\mathbf{x}_t))^{-1}(\mathbf{I} + \mathbf{S}(\mathbf{x}_t))$. In the main text we use matrix exponential as default option.

Crucially, the weights of the final linear layer of the MLP are initialized to exactly zero. Consequently, at the onset of training, the network outputs $\mathbf{S}(\mathbf{x}_t) = \mathbf{0}$, which yields $\mathbf{Q}(\mathbf{x}_t) = \mathbf{I}$. This initialization strategy guarantees that the joint training step begins precisely at the stable OLS baseline before gradually introducing the parameterized nonlinear dynamics.

b. Data standardization. Data standardization requires careful treatment, as the strict physical constraint of energy conservation (the L_2 norm) depends on the geometry of the original variables and is not generally preserved in a shifted and scaled coordinate space. To ensure numerical stability during optimization, the neural network emulator is trained on standardized variables, obtained by transforming each time series in \mathbf{x}_t to zero mean and unit variance:

$$\tilde{\mathbf{x}}_t = \Sigma_{\text{std}}^{-1}(\mathbf{x}_t - \boldsymbol{\mu}),$$

where $\boldsymbol{\mu}$ contains the empirical means and Σ_{std} is a diagonal matrix of standard deviations.

The orthogonal constraint on the nonlinear operator \mathbf{Q} is formulated to conserve energy exclusively in the physical space. Accordingly, while the neural network generating $\mathbf{Q}(\tilde{\mathbf{x}}_t)$ takes standardized inputs, the resulting rotation acts on the unstandardized physical state to yield an intermediate rotated state \mathbf{v}_t :

$$\mathbf{v}_t = \mathbf{Q}(\tilde{\mathbf{x}}_t)(\Sigma_{\text{std}}\tilde{\mathbf{x}}_t + \boldsymbol{\mu}).$$

We note that $\mathbf{Q}(\tilde{\mathbf{x}}_t)$ still acts on the standardized states $\tilde{\mathbf{x}}_t$ as it usually facilitate training. To apply the linear dynamics, this physically rotated state must be mapped back into the standardized coordinate space, effectively removing the physical offsets:

$$\tilde{\mathbf{v}}_t = \Sigma_{\text{std}}^{-1}(\mathbf{v}_t - \boldsymbol{\mu}).$$

Finally, the linear operator \mathbf{M} and the effective deterministic forcing \mathbf{F} (both parameterized in the standardized space) act on this standardized rotated state to yield the full discrete update:

$$\tilde{\mathbf{x}}_{t+1} = \mathbf{F} + \mathbf{M}\tilde{\mathbf{v}}_t.$$

This careful separation guarantees that the nonlinear interactions remain strictly energy-conserving with respect to the original physical variables, while the linear dissipation (and the neural network optimization) operate in a well-conditioned standardized space. Finally, we note that by virtue of standardizing the state variables to zero mean, the constant forcing vector \mathbf{F} is essentially zero at initialization and remains negligibly small during training.

c. Fitting the noise term. Once the deterministic discrete map \mathbf{f} is estimated, we close the model with a stochastic forcing. We compute the residuals of the deterministic dynamics as $\mathbf{r}_t = \mathbf{x}_{t+1} - \mathbf{f}(\mathbf{x}_t)$, with $\mathbf{r}_t \in \mathbb{R}^n$, and construct a stochastic parameterization based on these residuals. As the primary focus of this work is on constraining the deterministic drift, we adopt the simplest choice of additive diagonal noise: the diagonal matrix $\boldsymbol{\Sigma}$ with each entry computed as the standard deviation of the residual component $r_t^{(i)}$. More general stochastic parameterizations, including state-dependent and correlated noise, can be readily constructed from \mathbf{r}_t ; we refer to Appendix C of [31] for details. Finally, the proposed physics-constrained architectures can be naturally combined with multilevel regression strategies [24] to account for non-Markovian memory effects arising from unresolved scales, which we leave for future work.

C. Causal constraints

The physics-constrained networks detailed above can be augmented via a causal regularization term by adding a quadratic penalty to the MSE loss:

$$\begin{aligned} \mathcal{L} &= \mathcal{L}_{\text{MSE}} + \mathcal{L}_{\text{Causal}} \\ &= \text{MSE}(\mathbf{x}_{t+1}, \mathbf{f}(\mathbf{x}_t)) + \lambda \sum_{(k,j) \in \mathcal{S}} \left(\frac{\partial f_k}{\partial x^{(j)}} \right)^2, \end{aligned} \quad (6)$$

where the gradients $\frac{\partial f_k}{\partial x^{(j)}}$ are efficiently computed during training via automatic differentiation [91].

In the ideal case of recovering the exact causal graph, the purely quadratic penalty in Eq. (6) suffices to enforce the correct sparsity pattern in the discrete map’s Jacobian. However, in high-dimensional systems with finite data, causal estimates are inherently uncertain, and False Negatives (i.e. true causal couplings $x^{(j)} \rightarrow x^{(k)}$ mistakenly classified as non-causal) may occur. Under a strict quadratic penalty, such errors would severely bias the learned dynamics by artificially suppressing the required gradients.

To mitigate this, we propose a robust, capped penalty in the main text:

$$\mathcal{L}_{\text{Causal}}^{\text{Robust}} = \lambda \sum_{(k,j) \in \mathcal{S}} \min \left(\left(\frac{\partial f_k}{\partial x^{(j)}} \right)^2, \gamma \right). \quad (7)$$

This capped formulation strictly bounds the penalty. Once the squared gradient reaches the threshold γ , the derivative of the regularizer with respect to the network weights vanishes. Consequently, if the MSE loss strongly dictates that a specific coupling is necessary to predict \mathbf{x}_{t+1} (i.e., a mistakenly excluded interaction), the MSE term will easily overcome the bounded penalty. False Positives, by contrast, do not induce structural bias, as they are simply excluded from the set \mathcal{S} and thus unpenalized.

1. Heuristic for the “cap” parameter γ

We propose a heuristic to estimate the cap parameter γ directly from the discrete impulse response operator $R_1^{k,j}$ obtained via the FDT. The impulse response $R_t^{k,j}$ measures the change in variable $x^{(k)}$ at time step t following a small perturbation applied to $x^{(j)}$ at step 0. As described in the main text, direct causal links $x^{(j)} \rightarrow x^{(k)}$ are identified from the unit-step responses $R_1^{k,j}$ by: (i) applying a logarithmic transformation $\ln |R_1^{k,j}|$ for $k \neq j$, (ii) partitioning these values using k -means clustering ($k = 2$), and (iii) assigning a causal link to the cluster associated with the larger centroid. Let $\tilde{R}_1^{k,j}$ denote the subset of responses belonging to this cluster, corresponding to statistically significant (non-spurious) interactions. We define the cap parameter γ as a low quantile of these squared significant responses; in our experiments, we use the 0.1 quantile. This choice establishes a strict lower bound on the magnitude of reliably detectable causal interactions. If during training the MSE term drives a penalized gradient beyond this threshold, if the MSE term forces a penalized gradient to exceed this threshold, i.e. $(\partial f_k / \partial x^{(j)})^2 \geq \gamma$, this indicates that the interaction is likely inconsistent with the assumed absence of a causal link (i.e. we are dealing with a False Negative). In this regime, the capped loss effectively deactivates the penalty, allowing the dynamics to be governed by the MSE term rather than by a potentially incorrect causal constraint.

2. Implementation details for the causal constraint

Enforcing the causal penalty defined in Eq. (7) requires computing the Jacobian of the deterministic forward map in Eq. (3). However, backpropagation through $\mathbf{Q}(\mathbf{x}_t) = \exp(\mathbf{S}(\mathbf{x}_t))$ is computationally expensive.

Therefore to enforce the causal constraints efficiently, we construct a first-order proxy for the forward map through the skew-symmetric infinitesimal generator $\mathbf{S}(\mathbf{x}_t)$. By expanding the orthogonal map to first order, $\mathbf{Q}(\mathbf{x}_t) \approx \mathbf{I} + \mathbf{S}(\mathbf{x}_t)$, the deterministic update $\mathbf{M}\mathbf{Q}(\mathbf{x}_t)\mathbf{x}_t$ can be evaluated for the purpose of the Jacobian penalty as:

$$\tilde{\mathbf{f}}(\mathbf{x}_t) = \mathbf{M}\mathbf{x}_t + \mathbf{M}\mathbf{S}(\mathbf{x}_t)\mathbf{x}_t. \quad (8)$$

Constant forcing terms are ignored in this proxy, as their derivative with respect to the state is zero. Crucially this proxy is evaluated strictly to compute the gradients $\partial \tilde{f}_k / \partial x^{(j)}$ for the regularization term $\mathcal{L}_{\text{Causal}}^{\text{Robust}}$. The primary state prediction \mathbf{x}_{t+1} , and its associated MSE loss, are always computed using the exact, energy-conserving orthogonal map $\mathbf{M}\mathbf{Q}(\mathbf{x}_t)\mathbf{x}_t$. This dual-path approach allows us to bypass the differentiation of the matrix exponential entirely.

II. MATHEMATICAL ORIGIN OF THE DISCRETE MODEL AND A FEW EXAMPLES

The data-driven model proposed in this work is formulated and solved as discrete-time map and it is fundamentally designed to simulate coarse-grained, *effective* dynamics directly from data. To establish the theoretical grounding of

this discrete formulation, we first demonstrate its mathematical connection to continuous-time systems. We further reformulate two illustrative dynamical systems via the proposed formulation. Finally, we test the framework by learning the effective dynamics of severely sub-sampled trajectories of the Charney-DeVore dynamical systems considered in the main text, targeting a regime where data-driven continuous models can fail due to numerical instability. In summary, this Section targets the following objectives:

- *Formulation in the continuous limit.* To build mathematical intuition, we first examine the limit of small time steps ($\Delta t \rightarrow 0$). We show that the general discrete architecture proposed in the main text arises naturally from the continuous equations via a Lie–Trotter splitting procedure [64]. We then further highlight this connection with practical examples by focusing on two canonical systems:
 - *Deterministic “warm-up” with Lorenz-63.* We reformulate the Lorenz-63 equations [60] into a structure consistent with our discrete emulator, yielding an elegant geometric interpretation of its chaotic dynamics.
 - *Stochastic triad model.* We extend this geometric intuition to stochastic processes by reformulating a known triad model with energy-conserving nonlinearities into the proposed framework.
- *Effective coarse-grained dynamics (Charney–DeVore).* Finally, we demonstrate the primary use case of our method: stable learning from severely coarse-grained data. Using the Charney–DeVore model presented in the main text, we train the framework on trajectories subsampled every 100 and 500 integration steps. In this limit, both standard numerical integrators and physics-constrained, continuous data-driven models inevitably go unstable. By contrast, our learned discrete map acts as a stable emulator of the effective finite-time dynamics.

A. Connection to the continuous case: general stochastic processes

We consider the general abstract formulation arising when many turbulent flows are projected onto orthogonal bases, as discussed in the main text and at the start of this SM. We write this formulation as:

$$d\mathbf{x} = [\mathbf{F} + \mathbf{A}\mathbf{x} + \mathbf{S}(\mathbf{x})\mathbf{x}]dt + \Sigma d\mathbf{W}, \quad (9)$$

where \mathbf{W} is a standard Wiener process and $\mathbf{S}(\mathbf{x})$ is strictly skew-symmetric, leading to energy conservation of the nonlinear term. For details on the various terms, see Section I A. To map this continuous system to our proposed discrete-time architecture over a time step Δt , we apply a first-order operator splitting [64]. This splitting procedure consists of two steps: we first decompose the dynamics into a purely nonlinear, energy-conserving step, followed by a linear, forced, and stochastic step.

Step (a): Nonlinear rotation. We first isolate the nonlinear advection term:

$$d\mathbf{x}^{(1)} = \mathbf{S}(\mathbf{x}^{(1)})\mathbf{x}^{(1)}dt. \quad (10)$$

We approximate the solution over the interval $[t, t + \Delta t]$ by freezing the state dependence of \mathbf{S} at the beginning of the interval. Using the initial condition $\mathbf{x}^{(1)}(t) = \mathbf{x}_t$, this yields the approximate nonlinear update:

$$\mathbf{v}_t = \exp(\Delta t \mathbf{S}(\mathbf{x}_t))\mathbf{x}_t \equiv \mathbf{Q}(\mathbf{x}_t)\mathbf{x}_t. \quad (11)$$

Because $\mathbf{S}(\mathbf{x}_t)$ is skew-symmetric, its matrix exponential $\mathbf{Q}(\mathbf{x}_t)$ is strictly orthogonal ($\mathbf{Q}^T \mathbf{Q} = \mathbf{I}$). Thus, this step represents a pure rotation in state space that strictly preserves the L_2 -norm (energy). Analytically, this step incurs a $\mathcal{O}(\Delta t^2)$ truncation error.

Step (b): Linear, forced, and stochastic flow. Next, we use the rotated intermediate state \mathbf{v}_t as the initial condition for the remaining terms over the same time interval, leading to the linear SDE:

$$d\mathbf{x}^{(2)} = [\mathbf{A}\mathbf{x}^{(2)} + \mathbf{F}]dt + \Sigma d\mathbf{W}_t, \quad \text{with } \mathbf{x}^{(2)}(t) = \mathbf{v}_t. \quad (12)$$

Its exact solution over one time step is:

$$\mathbf{x}_{t+1} = e^{\mathbf{A}\Delta t}\mathbf{v}_t + \int_0^{\Delta t} e^{\mathbf{A}(\Delta t-s)}\mathbf{F}ds + \int_0^{\Delta t} e^{\mathbf{A}(\Delta t-s)}\Sigma d\mathbf{W}_s. \quad (13)$$

We identify the following terms:

- *Linear Operator*: $\mathbf{M} = e^{\mathbf{A}\Delta t}$. The term $e^{\mathbf{A}\Delta t}\mathbf{v}_t$ in Eq. (12) then represents the sequential update $\mathbf{M}\mathbf{Q}(\mathbf{x}_t)\mathbf{x}_t$ considered in the previous Sections.
- *Effective Deterministic Forcing*: $\mathbf{F}_{\text{discrete}} = \int_0^{\Delta t} e^{\mathbf{A}(\Delta t-s)}\mathbf{F} ds$. Assuming \mathbf{A} is invertible and that \mathbf{F} is a constant forcing, the solution of this integral is:

$$\mathbf{F}_{\text{discrete}} = \mathbf{A}^{-1}(e^{\mathbf{A}\Delta t} - \mathbf{I})\mathbf{F} = \mathbf{A}^{-1}(\mathbf{M} - \mathbf{I})\mathbf{F}. \quad (14)$$

- *Effective Stochastic Forcing*: $\Sigma_{\text{discrete}}\boldsymbol{\xi}_t = \int_0^{\Delta t} e^{\mathbf{A}(\Delta t-s)}\Sigma d\mathbf{W}_s$. The covariance matrix of this process can be written as:

$$\mathbf{C} = \Sigma_{\text{discrete}}\Sigma_{\text{discrete}}^{\text{T}} = \int_0^{\Delta t} e^{\mathbf{A}(\Delta t-s)}\Sigma\Sigma^{\text{T}}e^{\mathbf{A}^{\text{T}}(\Delta t-s)} ds,$$

where Σ_{discrete} is the lower-triangular Cholesky factor of \mathbf{C} , and $\boldsymbol{\xi}_t \sim \mathcal{N}(\mathbf{0}, \mathbf{I})$. Importantly, \mathbf{C} satisfies the Lyapunov matrix equation [92]:

$$\mathbf{A}\mathbf{C} + \mathbf{C}\mathbf{A}^{\text{T}} = \mathbf{M}\Sigma\Sigma^{\text{T}}\mathbf{M}^{\text{T}} - \Sigma\Sigma^{\text{T}}, \quad \mathbf{M} = e^{\mathbf{A}\Delta t}. \quad (15)$$

Thus, \mathbf{C} can be identified by numerically solving the Lyapunov equation above. The term Σ_{discrete} is then extracted via Cholesky decomposition of \mathbf{C} .

Combining these steps yields a split numerical approximation of the forward dynamics:

$$\mathbf{x}_{t+1} = \mathbf{F}_{\text{discrete}} + \mathbf{M}\mathbf{Q}(\mathbf{x}_t)\mathbf{x}_t + \Sigma_{\text{discrete}}\boldsymbol{\xi}_t. \quad (16)$$

Which correspond to the same formulation in Eq. (1) in the main text. This derivation is formally first-order accurate, with a local $\mathcal{O}(\Delta t^2)$ splitting error and it precisely mirrors the discrete model employed in the main text. In contrast, the data-driven formulation does not impose any explicit requirement on the temporal resolution and is tailored to fit the *effective* dynamics of the system at coarse-grained time scales, which can differ substantially from the underlying continuous dynamics. At the same time, it enforces the resolution-independent orthogonality constraint of the nonlinear update $\mathbf{Q}(\mathbf{x}_t)\mathbf{x}_t$, guaranteeing that the nonlinear term cannot induce spurious energy growth or decay.

1. Deterministic regime. Pedagogical example with the Lorenz-63 model

We now show how to reformulate the Lorenz-63 system [60] as in (16). In this simple first case, the dynamics will be governed by the update $\mathbf{x}_{t+1} = \mathbf{M}\mathbf{Q}(\mathbf{x}_t)\mathbf{x}_t$. The continuous equations governing the state $\mathbf{x} = (x, y, z)$ are given by:

$$\begin{aligned} \dot{x} &= \sigma(y - x), \\ \dot{y} &= x(\rho - z) - y, \\ \dot{z} &= xy - \beta z. \end{aligned} \quad (17)$$

We can exactly decompose these dynamics into a constant linear operator \mathbf{A} and a state-dependent, strictly skew-symmetric matrix $\mathbf{S}(\mathbf{x})$:

$$\dot{\mathbf{x}} = \underbrace{\begin{bmatrix} -\sigma & \sigma & 0 \\ \rho & -1 & 0 \\ 0 & 0 & -\beta \end{bmatrix}}_{\mathbf{A}} \begin{bmatrix} x \\ y \\ z \end{bmatrix} + \underbrace{\begin{bmatrix} 0 & 0 & 0 \\ 0 & 0 & -x \\ 0 & x & 0 \end{bmatrix}}_{\mathbf{S}(\mathbf{x})} \begin{bmatrix} x \\ y \\ z \end{bmatrix}. \quad (18)$$

Here, the constant linear matrix \mathbf{A} encapsulates the system's local instabilities as well as dissipation. The nonlinear interactions are entirely isolated within $\mathbf{S}(\mathbf{x})$. Because $\mathbf{S}(\mathbf{x})^{\text{T}} = -\mathbf{S}(\mathbf{x})$, the nonlinear term is strictly energy-preserving, satisfying $\mathbf{x}^{\text{T}}\mathbf{S}(\mathbf{x})\mathbf{x} = 0$. The application of Lie–Trotter operator splitting [64] as explained in the above Section II A, leads to

$$\mathbf{x}_{t+1} = \mathbf{M}\mathbf{Q}(\mathbf{x}_t)\mathbf{x}_t, \quad (19)$$

where $\mathbf{x}_t = (x_t, y_t, z_t)$, $\mathbf{M} = \exp(\Delta t \mathbf{A})$, and $\mathbf{Q}(\mathbf{x}_t) = \exp(\Delta t \mathbf{S}(\mathbf{x}_t))$. Given that the infinitesimal generator $\mathbf{S}(\mathbf{x}_t)$ is skew-symmetric, its matrix exponential $\mathbf{Q}(\mathbf{x}_t)$ is strictly orthogonal. The nonlinear update matrix $\mathbf{Q}(\mathbf{x}_t)$ of the Lorenz-63 system can be calculated analytically and it is equal to:

$$\mathbf{Q}(\mathbf{x}_t) = \exp(\Delta t \mathbf{S}(\mathbf{x}_t)) = \begin{bmatrix} 1 & 0 & 0 \\ 0 & \cos(x_t \Delta t) & -\sin(x_t \Delta t) \\ 0 & \sin(x_t \Delta t) & \cos(x_t \Delta t) \end{bmatrix} \quad (20)$$

The linear operator \mathbf{M} can be computed numerically once a Δt is specified. For a chosen time step (e.g., $\Delta t = 0.01$) and standard Lorenz parameters ($\sigma = 10, \rho = 28, \beta = 8/3$), this evaluates to a constant matrix:

$$\mathbf{M} = \exp(\Delta t \mathbf{A})_{\Delta t=0.01} = \begin{bmatrix} 0.917925 & 0.0951229 & 0 \\ 0.266344 & 1.00354 & 0 \\ 0 & 0 & 0.973686 \end{bmatrix} \quad (21)$$

Given an initial condition $\mathbf{x}_{t=0}$, the discrete mapping explicitly factors the dynamics into two sequential geometric operations. First, the state-dependent orthogonal update $\mathbf{v}_t = \mathbf{Q}(\mathbf{x}_t)\mathbf{x}_t$ applies an energy-preserving rotation strictly in the y - z plane. The rotation angle $\theta = x_t \Delta t$ is state-dependent and dictated by the instantaneous intensity of the x_t coordinate, so nearby trajectories experience different rotations. Second, the linear transformation $\mathbf{x}_{t+1} = \mathbf{M}\mathbf{v}_t$ stretches and contracts the rotated vector \mathbf{v}_t . Crucially, unlike a purely dissipative operator, in the Lorenz system, \mathbf{M} is not contractive in its norm: it expands some directions while contracting others, making it a special case in respect to the class of systems considered in this study.

A long integration of this map reproduces the Lorenz attractor with high-fidelity, see Figure 1. The code to reproduce such results can be found in the code availability Section in the main text.

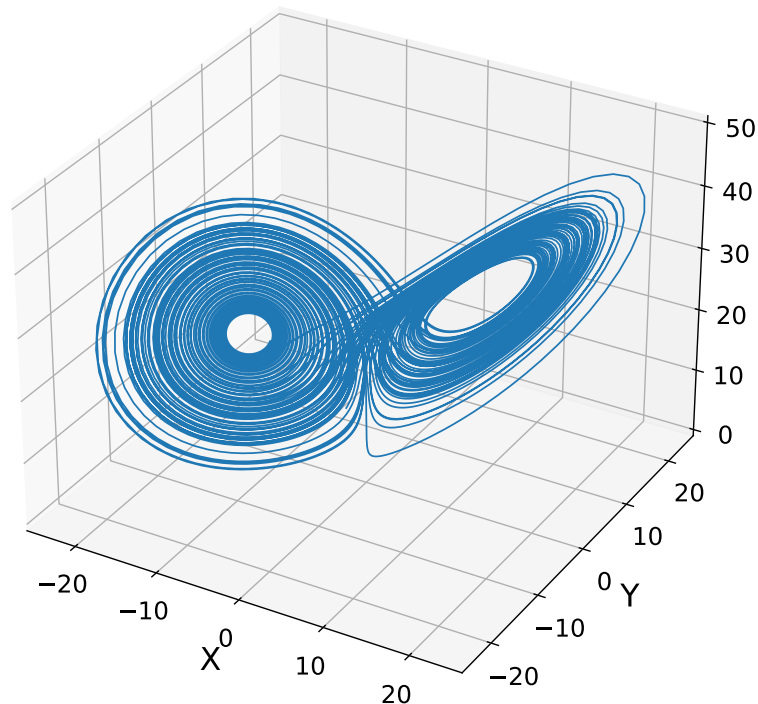


FIG. 1: Lorenz attractor simulated with the sequential mapping scheme $x_{t+1} = \mathbf{M}\mathbf{Q}(\mathbf{x}_t)\mathbf{x}_t$.

2. Stochastic regime. Pedagogical example with triad models

We now consider the stochastic triad model proposed in [9] and formulated as:

$$\begin{aligned} dx_1 &= L_2x_3 - L_3x_2 - d_1x_1 + B_1x_2x_3 + F_1 + \sigma_1dW_1, \\ dx_2 &= L_3x_1 - L_1x_3 - d_2x_2 + B_2x_1x_3 + F_2 + \sigma_2dW_2 \\ dx_3 &= L_1x_2 - L_2x_1 - d_3x_3 + B_3x_1x_2 + F_3 + \sigma_3dW_3. \end{aligned} \quad (22)$$

This model serves as a fundamental building block for complex turbulent dynamical systems, as three-dimensional Galerkin truncations of various fluid equations naturally yield this structural form (see Chapter 2 of Ref. [2]). The linear operator \mathbf{A} can be decomposed in $\mathbf{A} = \mathbf{L} + \mathbf{D}$, where \mathbf{L} is a skew-symmetric matrix representing dispersion, and \mathbf{D} is a symmetric negative-definite matrix representing dissipation. In the specific case in Eq. (22), \mathbf{D} is diagonal and the components d_i are strictly positive. \mathbf{W} is the standard Wiener process. The quadratic nonlinearities are energy conserving satisfying the condition $\mathbf{x} \cdot \mathbf{B}(\mathbf{x}, \mathbf{x}) = 0$. This property explicitly imposes the constraint $B_1 + B_2 + B_3 = 0$ on the nonlinear coefficients.

The model can be naturally cast into the general stochastic differential equation form introduced in Eq. (9):

$$\begin{bmatrix} dx_1 \\ dx_2 \\ dx_3 \end{bmatrix} = \left(\underbrace{\begin{bmatrix} F_1 \\ F_2 \\ F_3 \end{bmatrix}}_{\mathbf{F}} + \underbrace{\begin{bmatrix} -d_1 & -L_3 & L_2 \\ L_3 & -d_2 & -L_1 \\ -L_2 & L_1 & -d_3 \end{bmatrix}}_{\mathbf{A}} \begin{bmatrix} x_1 \\ x_2 \\ x_3 \end{bmatrix} + \underbrace{\begin{bmatrix} 0 & B_1x_3 & 0 \\ -B_1x_3 & 0 & -B_3x_1 \\ 0 & B_3x_1 & 0 \end{bmatrix}}_{\mathbf{S}(\mathbf{x})} \begin{bmatrix} x_1 \\ x_2 \\ x_3 \end{bmatrix} \right) dt + \underbrace{\begin{bmatrix} \sigma_1 & 0 & 0 \\ 0 & \sigma_2 & 0 \\ 0 & 0 & \sigma_3 \end{bmatrix}}_{\mathbf{\Sigma}} \begin{bmatrix} dW_1 \\ dW_2 \\ dW_3 \end{bmatrix}, \quad (23)$$

with $B_2 = -(B_1 + B_3)$. $\mathbf{S}(\mathbf{x})$ is skew-symmetric, and therefore energy conserving.

Performance of the approximation in a regime with dual energy cascade. We now test the relevance of the splitting procedure in Eq. (16) in the stochastic context. We follow Majda and Qi [9] and consider a set of parameters leading to a dual energy cascade across modes x_1 , x_2 , and x_3 . Specifically, we set $d_1 = 1$, $d_2 = d_3 = 2$; $\sigma_1^2 = 10$, $\sigma_2^2 = \sigma_3^2 = 0.01$. The nonlinear coefficients are $B_1 = 2$, $B_2 = B_3 = -1$. The linear interactions are set to $L_1 = 0.09$, $L_2 = 0.06$, and $L_3 = -0.03$. The deterministic forcing is applied only to the x_2 and x_3 modes, such that $F_1 = 0$, $F_2 = -1$, and $F_3 = 1$. Given the chosen parameters, the x_1 mode is subject to strong stochastic forcing, while x_2 and x_3 are less energetic. The quadratic nonlinear coupling $\mathbf{B}(\mathbf{x}, \mathbf{x})$ redistributes this energy, creating a cascade from the highly energetic x_1 mode to the less energetic x_2 and x_3 modes. Conversely, the deterministic forcing applied to x_2 and x_3 drives a backward energy cascade towards x_1 . Therefore, these parameters place the system in a complex, dual energy cascade regime.

We simulate the dynamics using the proposed splitting procedure for stochastic systems as in Eq. (16) and compare it to a standard Euler-Maruyama scheme. The simulation length is 5×10^7 time steps with a step size of $\Delta t = 0.001$. Importantly, the effective deterministic forcing $\mathbf{F}_{\text{discrete}}$ and the effective stochastic forcing $\mathbf{\Sigma}_{\text{discrete}}\boldsymbol{\xi}_t$ in Eq. (16) are derived following the steps proposed in Section II A: $\mathbf{F}_{\text{discrete}} = \mathbf{A}^{-1}(\mathbf{M} - \mathbf{I})\mathbf{F}$, and the covariance for $\mathbf{\Sigma}_{\text{discrete}}$ is obtained by solving the associated continuous Lyapunov equation. In Figure 2, we show the stationary distributions of the x_1 , x_2 , and x_3 modes, plotted against a Gaussian distribution with the same mean and variance for reference. The two simulations reconstruct the identical stationary statistics and are both in good agreement with the results of Majda and Qi (see Figure 4.1C in Ref. [9]).

This result further motivates Eq. (16) as a robust scheme to reproduce trustworthy statistics in the continuous limit $\Delta t \rightarrow 0$ beyond deterministic systems, successfully extending to forced stochastic systems. In the next section, we return to the data-driven setting and demonstrate that learning neural models constrained by the formulation in Eq. (16) yields skillful emulators even from severely sub-sampled data, a regime where both standard numerical integrators and (physics constrained) continuous-time data-driven models fail.

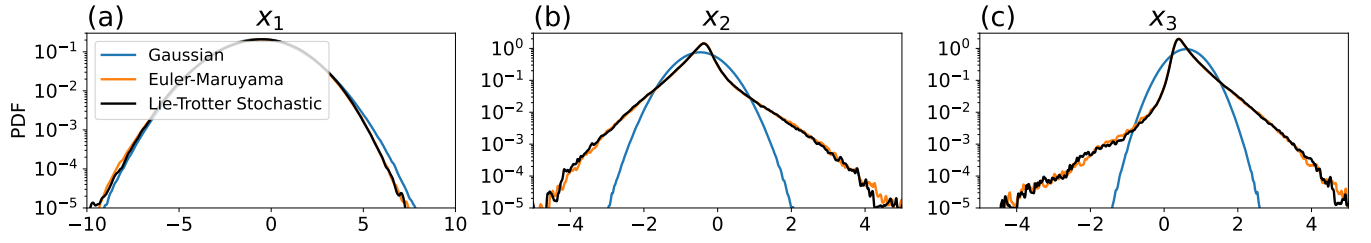


FIG. 2: Stationary distributions (PDFs) of x_1 , x_2 , and x_3 in the triad model, simulated by a standard Euler-Maruyama scheme and our Lie-Trotter splitting procedure $\mathbf{x}_{t+1} = \mathbf{F}_{\text{discrete}} + \mathbf{M}\mathbf{Q}(\mathbf{x}_t)\mathbf{x}_t + \mathbf{\Sigma}_{\text{discrete}}\boldsymbol{\xi}_t$. The deterministic and stochastic forcings, $\mathbf{F}_{\text{discrete}}$ and $\mathbf{\Sigma}_{\text{discrete}}\boldsymbol{\xi}_t$, are derived analytically via the steps proposed in Section II A. PDFs are plotted on a logarithmic scale. A Gaussian distribution with the same mean and variance as the Euler-Maruyama results is provided for reference.

B. Data-driven emulation of the Charney-DeVore model from subsampled data

We return to the Charney-DeVore model [58] introduced in Eq. (5) of the main text. In the main manuscript, the emulator was learned from a well-sampled trajectory to allow for a direct statistical comparison with the continuous model. However, our proposed neural model can operate in sparse observational regimes where standard numerical integrators fail. To demonstrate this, we evaluate our architecture in two coarse-grained regimes:

- *Subsampling every 100 time steps.* We consider a long integration ($T = 10^7$ time steps) $\mathbf{x}_t \in \mathbb{R}^{n,T}$ of the Charney-DeVore model as in the main text. This integration was generated with an Euler-Maruyama scheme and $\Delta t = 0.01$. We then subsample the data by considering every 100th time step. This corresponds to observing the data every $\Delta t = 1$. We refer to this new subsampled trajectory as $\tilde{\mathbf{x}}_t$. We train the proposed discrete neural emulator in Eq. (3), with energy-conserving nonlinearities, from $\tilde{\mathbf{x}}_t$. We then assess the stationary distributions (PDFs) and autocorrelation functions (ACFs) of variables $\tilde{x}_t^{(1)}, \tilde{x}_t^{(2)}, \dots, \tilde{x}_t^{(6)}$ and show the results in Figure 3. Our discrete emulator remains strictly stable and successfully learns the effective discrete mapping. On the other hand, the numerical integrator blows up with $\Delta t = 1$. Furthermore, data-driven models with physics constrained defined in the continuous limit also become unstable.
- *Subsampling every 500 time steps.* We further challenge the framework by subsampling the original time series every 500 steps. This reduces the amount of available data for training to 20,000 time points. Despite this, the PDFs and ACFs of the learned discrete mapping remain generally well-approximated (Figure 4). The largest error is found for the PDFs of the x_2 degree of freedom. Most importantly, the neural emulator guarantees stability, providing a robust finite-time flow map in a regime where traditional integration schemes fail.

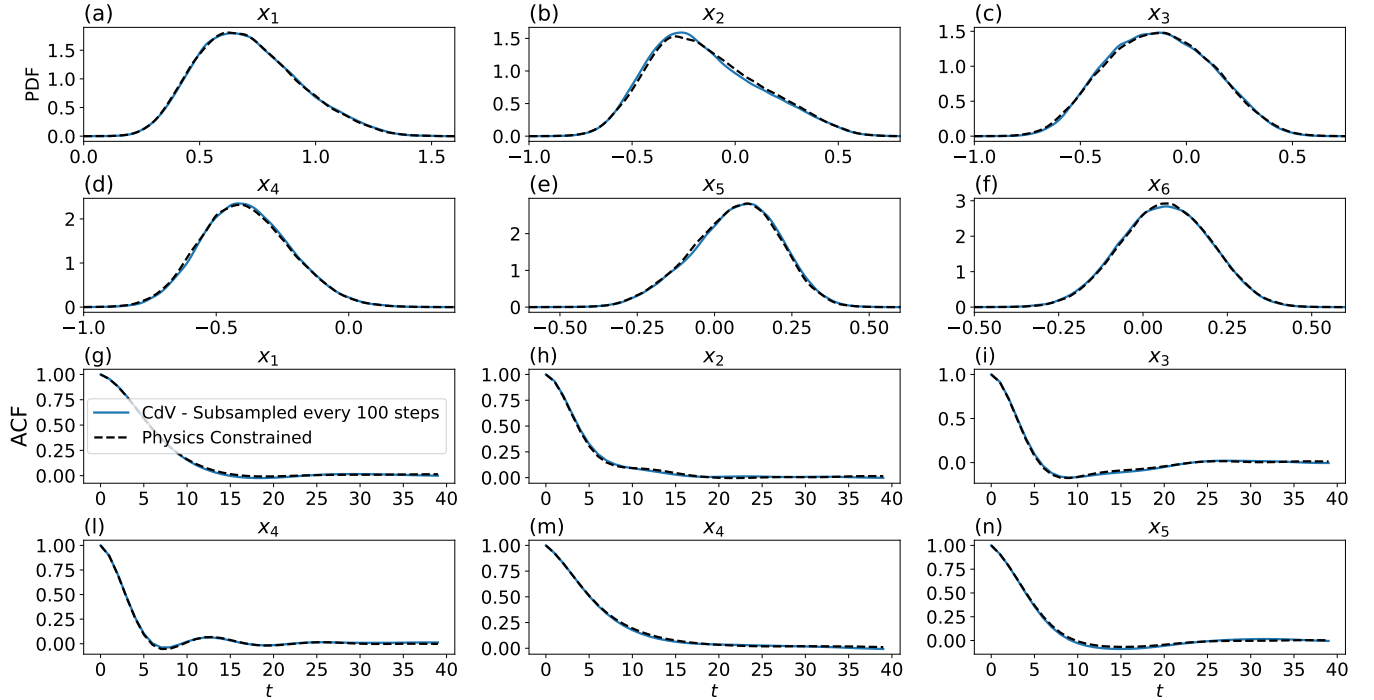


FIG. 3: Experiment with subsampling size 100. In the first and second rows, we show the stationary distributions (PDFs) of the variables $\tilde{x}_t^{(1)}, \tilde{x}_t^{(2)}, \dots, \tilde{x}_t^{(n)}$ of the physics-constrained emulator and the subsampled time series $\tilde{\mathbf{x}}_t$. In the third and fourth rows, same as the first two rows but for the autocorrelation functions (ACFs). Note: a numerical solution at this coarse-grained temporal resolution does not exist (the numerical model blows up at $\Delta t = 1$).

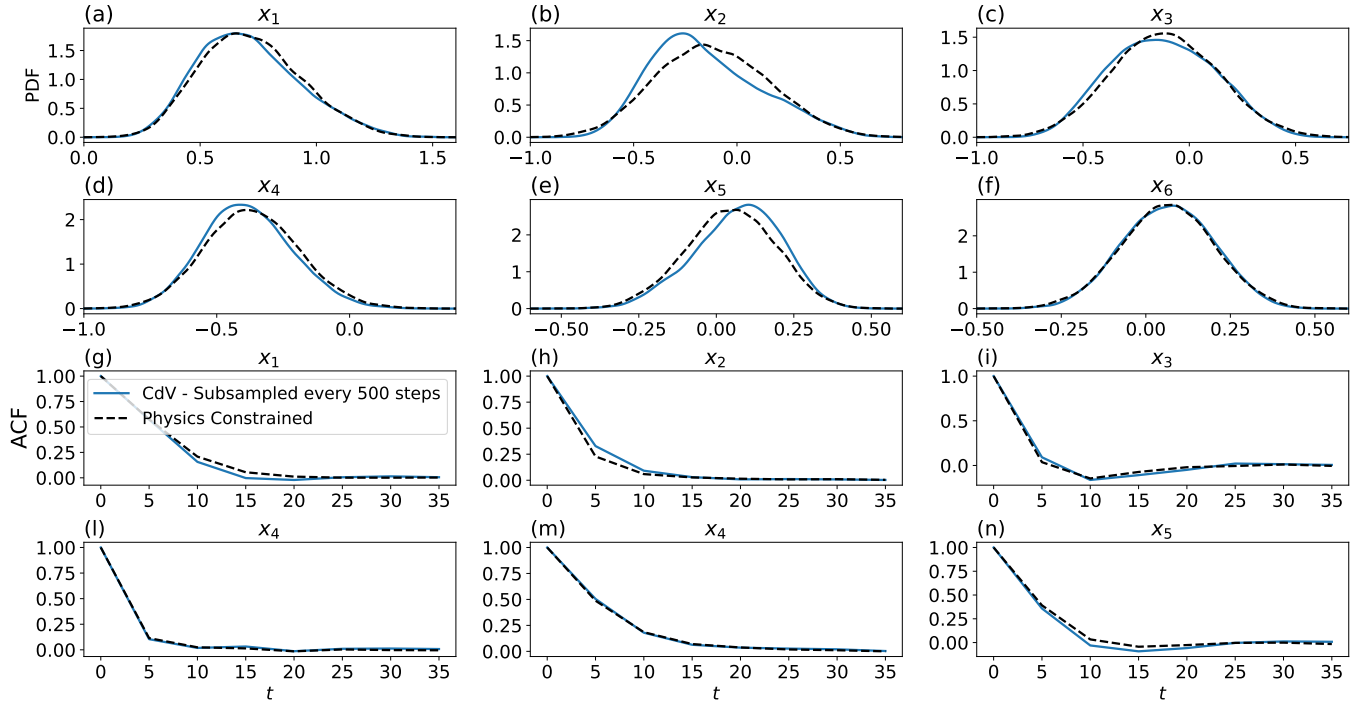


FIG. 4: Same as Fig. 3 but after subsampling the original Charney-DeVore integration every 500 time steps (corresponding to $dt = 5$). Note: a numerical solution at this coarse-grained temporal resolution does not exist (the numerical model blows-up at $dt = 5$).

III. FLUCTUATION-DISSIPATION THEOREM (FDT) FROM DATA: QUASI-GAUSSIAN AND SCORE MATCHING

The FDT. Consider a n -dimensional system $\mathbf{x}_t = (x_t^{(1)}, x_t^{(2)}, \dots, x_t^{(n)})$. The Fluctuation-Dissipation Theorem (FDT) states that the time-dependent response of an observable $A(x_t^{(k)})$ to a small impulse perturbation $\delta x_0^{(j)}$ imposed on $x_{t=0}^{(j)}$ at time $t = 0$, can be retrieved solely from stationary statistics of the system as:

$$R_t^{k,j} = \lim_{\delta x_0^{(j)} \rightarrow 0} \frac{\delta \langle A(x_t^{(k)}) \rangle}{\delta x_0^{(j)}} = - \left\langle A(x_t^{(k)}) \frac{\partial \ln \rho(\mathbf{x})}{\partial x^{(j)}} \Big|_{\mathbf{x}_0} \right\rangle. \quad (24)$$

where $\rho(\mathbf{x})$ represents the invariant probability distribution of the system [65, 93]. The FDT establishes a link between perturbed quantities and stationary statistics, i.e. the invariant measure of the system [54, 65]. The brackets $\langle \cdot \rangle$ represents ensemble averages, in practice computed using temporal averages under the assumption of ergodicity. Application of the FDT in the main text focused on the observable $A(x_t^{(k)}) = x_t^{(k)}$. In this case, Eq. 2 represents the impulse response in the ensemble mean.

A. The FDT from data

Quasi-Gaussian (qG) approximation. A long standing problem in inferring the FDT response operator is the need to estimate the gradients of logarithm of the invariant distribution $s(\mathbf{x}) = \nabla \ln \rho(\mathbf{x})$, the so-called *score function* [75]. Traditionally, the quasi-Gaussian (qG) approximation has been used [54, 74], by replacing $\rho(\mathbf{x})$ by a Gaussian distribution $\rho^G(\mathbf{x})$ with the same mean and second moments. In this case the score can be directly is:

$$s^G(\mathbf{x}) = \nabla \ln \rho^G(\mathbf{x}) = -\Sigma^{-1}(\mathbf{x} - \boldsymbol{\mu}). \quad (25)$$

$\boldsymbol{\mu} \in \mathbb{R}^n$ and $\Sigma \in \mathbb{R}^{n,n}$ are the mean and covariance matrix of the data, respectively. Note, that while a Gaussian approximation is used for $\rho(\mathbf{x})$, the response formula in Eq. (24) is still computed over the original invariant measure [54, 67]. In other words, this approximation differs from linear inverse model strategies

which assume a Gaussian measure from the outset. The qG approximation has high skill in predicting responses in the ensemble mean even in nonlinear systems [54, 56, 94] but it can introduce biases for higher order moments [67, 95].

Score-based generative modeling and FDT. Recent advances in generative modeling provide novel tools for estimating the score function directly from data, overcoming assumptions such as the qG approximation. In particular, [68] showed that score estimation can be recasted as a denoising problem. This led to scalable diffusion models that integrate a reverse-time Langevin equation from a reference distribution (typically Gaussian) toward the data distribution [43]. As in the FDT framework, a central object of these frameworks is the score function. Giorgini et al. (2024) [66], first proposed to use denoising score matching strategies in the FDT context. In practice, the true score on the system’s attractor can be then approximated by the score of a distribution perturbed with a small amount of noise [66]. This strategy has been successfully applied to stochastic dynamical systems of increasing complexity [66, 67]. The broader appeal of this approach is its connection between established ideas from statistical physics (FDT) and modern generative modeling.

Score matching. In this study, we extended the prior work in [66, 67] by learning the score directly on the attractor using the classic result of Hyvärinen (2005) [75], hereafter “score matching”. Given T samples of a n dimensional dynamical system $\mathbf{x} \in \mathbb{R}^{T,n}$, we parameterize the score function $s_\theta(\mathbf{x})$ with a neural network s and parameters θ . Specifically, s_θ is approximated with a multilayer perceptron (MLP). The network is trained by minimizing the following loss:

$$\mathbb{E}_{\rho(x)}[\text{tr}(\nabla_{\mathbf{x}} s_\theta(\mathbf{x})) + \frac{1}{2} \|s_\theta(\mathbf{x})\|_2^2], \quad (26)$$

where the expectation $\mathbb{E}_{\rho(x)}$ is approximated by a time average over the available samples. The specific implementation used in this work relies on an approximation similar to the sliced score-matching approach proposed in [69]. Specifically, we considered the Hutchinson Trace Estimation [96] to compute the trace in Eq. (26). As in Giorgini et al. (2025) [67], in the case of high-dimensional dynamics we suggest using the common denoising score matching implemented with a U-Net architecture.

Practical considerations and correction procedure. The score-matching procedure introduced by Hyvärinen (2005) [75] provides an elegant way to estimate the score $s(\mathbf{x})$ directly on the system’s inertial manifold. In practice, however, this estimation can be prone to several sources of error. First, ensemble averages must be replaced by empirical averages computed from finite datasets. Second, the inferred score inevitably depends on the chosen neural-network architecture and its associated hyperparameters. Nevertheless, the theoretical formalism of the FDT, provides analytical constraints on the instantaneous response $\mathbf{R}_{t=0}$. As shown in [66], these constraints can be used as a posteriori correction of the estimated score, thereby ensuring reliable results. Such corrections are non-unique, but they typically produce only small adjustments to the inferred response and thus eliminate the need for more sophisticated architectures. In what follows, we detail the analytical correction for score-based estimates relevant to the ensemble-mean response. We denote the ideal score by $s(\mathbf{x})$, the score inferred through score matching by $s_\epsilon(\mathbf{x})$, and the corrected score by $s_c(\mathbf{x})$. The system’s dynamics is encoded in a data matrix $\mathbf{x} \in \mathbb{R}^{T,n}$, where T is the number of temporal samples and n the system’s dimensionality. The correction procedure is dependent on the type of response analyzed. If the interest is in the response in ensemble mean, i.e. observable $A(x_t^{(k)}) = x_t^{(k)}$ in Eq. (24), then it is possible to use the correction already outlined in [66]. The response operator in the ensemble mean at time $t = 0$ of any system is:

$$\mathbf{R}_0 = \mathbf{I} \quad (27)$$

\mathbf{I} being the identity matrix. The empirical estimation of the instantaneous response operator with the inferred score $\tilde{s}(\mathbf{x})$ will lead to small errors, so that

$$\tilde{\mathbf{R}}_0 = -\frac{1}{T} \mathbf{x}^T \cdot \tilde{s}(\mathbf{x}) = \mathbf{I} - \epsilon \quad (28)$$

where $\tilde{\mathbf{R}}_0$ denotes the estimated response. It is then possible to correct the inferred score as:

$$s_c(\mathbf{x}) = \tilde{s}(\mathbf{x}) \cdot (\mathbf{I} - \epsilon)^{-1}. \quad (29)$$

The corrected score $s_c(\mathbf{x})$ defined in Eq. (29) guarantees the equivalence Eq. (27) and it is the one used in the computation of responses in ensemble mean in the main text. Note that while this correction is non-unique, different versions lead to small differences as argued in the SM of [28].

Crucially, depending on the data, it may be useful to compute the response $R_t^{k,j}$ on standardized data. This is especially true when variables span disparate scales, as in principal component representations.

Response operator via score matching: response in the ensemble mean. Given the proposed correction in Eq. (29), we now infer the response operator for the Charney-DeVore system in Eq. (3) in the main text. We compare the prediction of the qG approximation and the score-matching estimation against the numerical ground truth and show the results in Figure 5. First, we note that the quasi-Gaussian approximation leads to good, first-order results even in a strongly nonlinear model such as the Charney-DeVore model. The FDT inferred through score matching is generally more accurate than the quasi-Gaussian approximation.

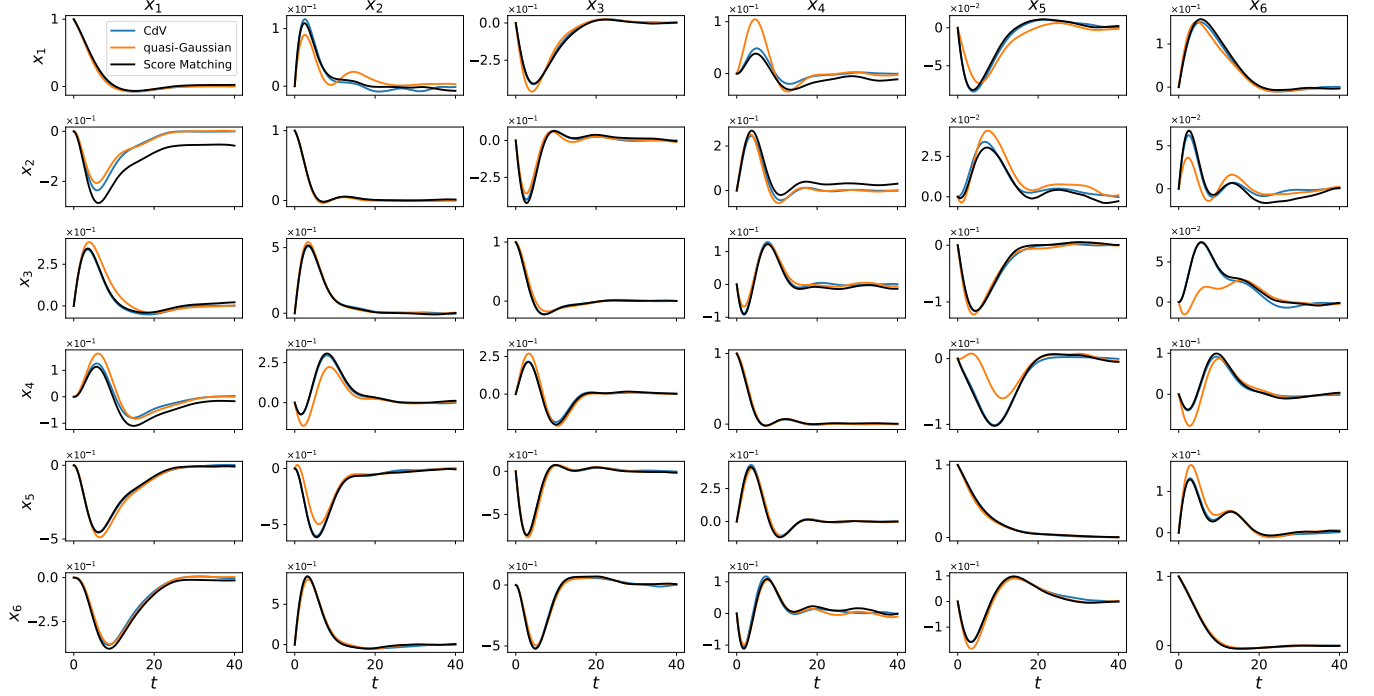


FIG. 5: Time-dependent, responses in ensemble mean $x_t^{(k)}$ to an impulse perturbation in the CdV model (Eq. (3) in the main text) as predicted by the FDT using the quasi-Gaussian and score-matching approximations. Example: column (1), row (2) quantifies the time-dependent mean response of $x_t^{k=2}$ given a small, impulse perturbation imposed on $x_0^{j=1}$ at time $t = 0$.

IV. POSSIBLE LIMITATIONS OF THE CAUSAL CONSTRAINTS AND PRACTICAL CONSIDERATIONS

Causal relations in high-dimensional stochastic dynamical systems are most naturally, and practically, identified at the level of ensemble-averaged quantities [31]. Accordingly, the causal constraints introduced in the main text, exploit vanishing entries of the ensemble-averaged Jacobian, $\langle \partial f_k(\mathbf{x})/\partial x^{(j)} \rangle = 0$, to suppress the corresponding state-dependent couplings $\partial f_k(\mathbf{x})/\partial x^{(j)}$ in the neural network loss.

A complication can in principle arise in idealized systems with exact symmetries, such as the Lorenz '63 and Lorenz '96 systems [59, 60]. In such cases $R_1^{k,j} = 0$ can arise from exact cancellations in the ensemble average, even though $\partial f_k(\mathbf{x})/\partial x^{(j)} \neq 0$ pointwise. One possible strategy in such idealized settings is to explicitly reduce the symmetries of the underlying dynamical system, following symmetry-reduction approaches advocated in [77]. For example, Ref. [78] proposed a nonlinear coordinate transformation to quotient the Z_2 symmetry of the Lorenz '63 system [60], leading to the so-called ‘‘proto-Lorenz’’ system. The limitation discussed above does not constitute a practical obstacle for reduced-order modeling of realistic, complex turbulent dynamical systems. In these realistic flows, symmetries are always broken.

Assessment of causal constraints. Crucially, as also noted in the main text, differently from the rigid (data independent) physical constraints, the utility of causal constraints depends on the system under study and on the accuracy of the data-driven causal discovery. The benefit of augmenting physics-constrained models with causal information can be assessed directly from data by comparing the FDT-based operator with the emulators’ response operators. Such comparisons should be performed at short time lags to avoid spurious responses that may arise at longer lags when using the FDT [97]. The causal constraints introduced here should be applied when they improve the representation of the response operator relative to the unconstrained model. In systems with exact symmetries, as discussed above, any biases introduced by the constraints will be immediately apparent in the representation of stationary variability.

V. CHARNEY DE-VORE MODEL: PARAMETERS

The values of the parameters used for the Charney-DeVore model (Eq. (3) in the main text) are reported in Table I below. All parameters are chosen with standard values as discussed in [67, 79, 81, 82]. The system is integrated using a Euler-Maruyama scheme with $dt = 0.01$.

TABLE I: Model coefficients for the six-dimensional stochastic Charney-DeVore model.

Parameter	Value	Description
C	0.1	Newtonian relaxation rate
x_1^*	0.95	Zonal background forcing (mode 1)
x_4^*	-0.76095	Zonal background forcing (mode 4)
γ	0.2	Topographic height
b	1.6	Channel aspect ratio
α_m	$\frac{8\sqrt{2}}{\pi} \frac{m^2}{4m^2-1} \frac{b^2+m^2-1}{b^2+m^2}$	Nonlinear advection (mode m)
β_m	$\frac{\beta b^2}{b^2+m^2}$	Coriolis effects (mode m)
δ_m	$\frac{64\sqrt{2}}{15\pi} \frac{b^2+m^2+1}{b^2+m^2}$	Triad interaction (mode m)
γ_m	$\gamma \frac{4m^3}{4m^2-1} \frac{\sqrt{2}b}{\pi(b^2+m^2)}$	Orographic damping (mode m)
$\tilde{\gamma}_m^*$	$\gamma \frac{4m}{4m^2-1} \frac{\sqrt{2}b}{\pi}$	Orographic forcing (mode m)
ε	$\frac{16\sqrt{2}}{5\pi}$	Wave-wave interaction
σ	0.05	Noise amplitude
dt	0.01	Integration time step

VI. PRACTICAL ESTIMATION OF THE RESPONSE OPERATOR

To estimate the response operator in practice we follow the steps proposed in Appendix A of Falasca (2025) [31]. We report those steps here for completeness.

Given a model $\mathbf{x}_{t+1} = \mathbf{f}(\mathbf{x}_t) + \Sigma \boldsymbol{\xi}(t)$, we build the impulse response operator as follows:

1. We simulate a very long trajectory of the model, starting from a random initial condition and remove an initial transient. We then sample N_e random points from the simulation to define an ensemble of N_e initial conditions on the model's attractor. N_e should be very large (i.e. $N_e \gg 1$) in order to sample the whole attractor and approximate averages over the invariant distribution. Here we chose $N_e = 10^6$ members.
2. For each one of the N_e initial conditions, we impose an impulse perturbation Δ_j to the degree of freedom $x^{(j)}$ at time $t = 0$. The amplitude of the perturbation should be theoretically infinitesimally small, ensuring linearity of the response even in nonlinear systems. In practice we do as follows: we consider the long time series of $x_t^{(j)}$ from the long control integration above and define $\Delta_j = 10^{-2} \sigma_j$, where σ_j is the standard deviation of time series $x_t^{(j)}$.
3. Therefore, for a given initial condition \mathbf{x}_0 , we simulate two trajectories: a control trajectory without perturbation and a perturbed one, where an impulse perturbation Δ_j has been imposed on the j -th degree of freedom at time $t = 0$. This procedure is repeated in parallel for all initial conditions, resulting in an ensemble of N_e paired of control and perturbed trajectories.
4. At each time t we then estimate the time dependent ensemble average $\langle A(x_t^{(k)}) \rangle$ of an observable $A(x_t^{(k)})$ for both the perturbed and unperturbed run. We refer to the perturbed and control ensemble average respectively as $\langle A(x_t^{(k)}) \rangle_P$ and $\langle A(x_t^{(k)}) \rangle$. The observables considered in this study are going to be: (i) $A(x_t^{(k)}) = x_t^{(k)}$ and (ii) $A(x_t^{(k)}) = (x_t^{(k)} - \mu_t^{(k)})^2$, with μ_t representing the time-dependent mean of the distribution, therefore quantifying the response in ensemble mean and variance.
5. We define the impulse response operator for observable $A(x_t^{(k)})$ as

$$R_t^{k,j} = \frac{\langle A(x_t^{(k)}) \rangle_P - \langle A(x_t^{(k)}) \rangle}{\Delta_j}.$$

VII. NEURAL EMULATORS OF THE CHARNEY-DEVORE MODEL: STATIONARY STATISTICS

Stationary density and autocorrelation functions of the Charney-deVore system as given by the numerical model, the vanilla emulator and the causal emulator.

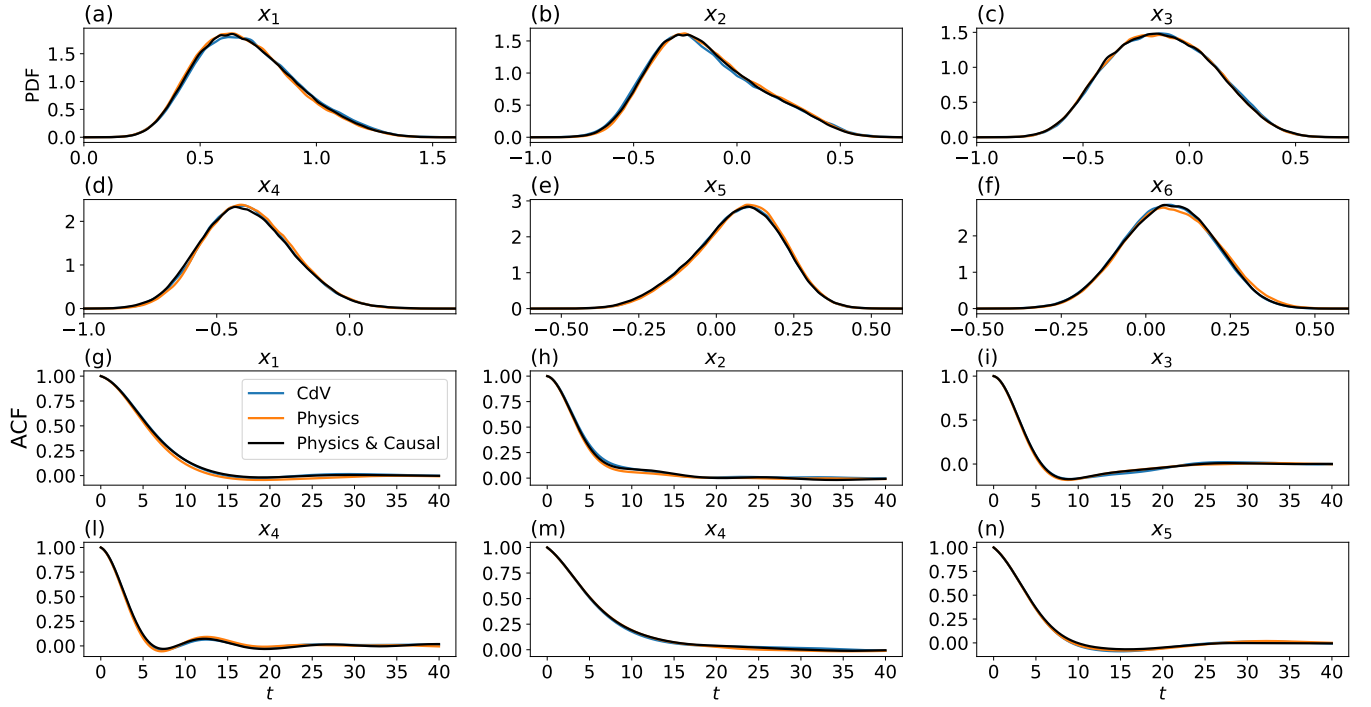


FIG. 6: Stationary statistics. First and second rows: stationary distributions (PDFs) of the variables $x^{(1)}, \dots, x^{(6)}$ of the CdV model. Labels: “CdV” refers to the numerical model; “Physics” is the model with only physics constrained; “Physics & Causal” is the model constrained by both physics and causal information. Third and fourth rows: same as the first row but for the autocorrelation functions (ACFs).

VIII. RESPONSE OPERATOR FOR THE CHARNEY-DEVORE MODEL

In Figure 7 and Figure 8, we report the estimation of the full response operator in ensemble mean and variance as obtained by the numerical model and the two emulators. The response operators have been computed with the method presented in Section V and using $N_e = 10^6$ ensemble members. The unconstrained, vanilla emulator provides a very good representation of responses to impulse perturbations, as expected given the large training dataset and Markovianity of the system [31]. The causally constrained emulator yields a systematically improved representation of both mean and variance responses. This is further quantified by the total time-dependent MSE, aggregated over all j and k , between the emulators and the ground truth. This analysis is shown in Figure 9.

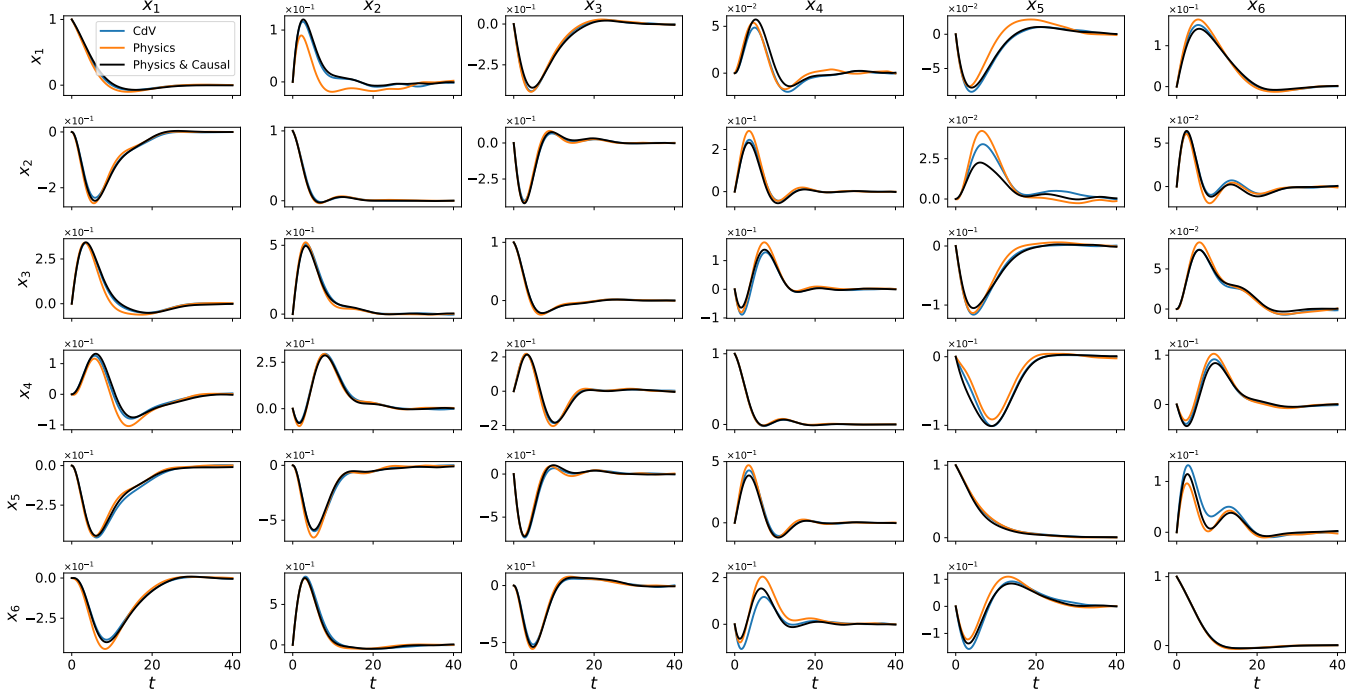


FIG. 7: Time-dependent, responses in ensemble mean of variable $x_t^{(k)}$ to an impulse perturbation the CdV model in Eq. (3) in the main text as predicted by the unconstrained and causally constrained emulators. Example: column (1), row (2) represents what is the time-dependent response of $x_t^{(k=2)}$ given a small, impulse perturbation imposed on $x_0^{(j=1)}$ at time $t = 0$. Labels: “CdV” refers to the numerical model; “Physics” is the model with only physics constrained; “Physics & Causal” is the model constrained by both physics and causal information.

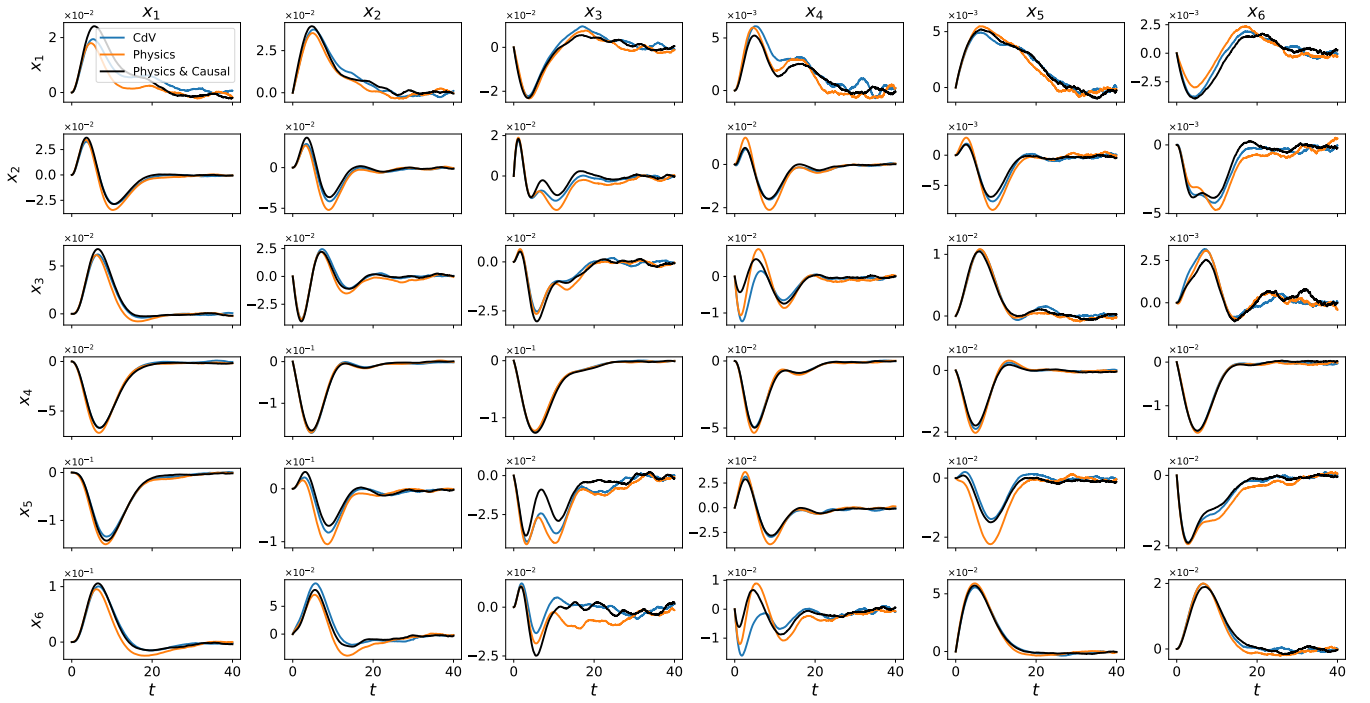


FIG. 8: Time-dependent, responses in ensemble variance of variable $x_t^{(k)}$ to an impulse perturbation the CdV model in Eq. (3) in the main text as predicted by the unconstrained and causally constrained emulators. Example: column (1), row (2) represents what is the time-dependent response of $x_t^{(k=2)}$ given a small, impulse perturbation imposed on $x_0^{(j=1)}$ at time $t = 0$. Labels: “CdV” refers to the numerical model; “Physics” is the model with only physics constrained; “Physics & Causal” is the model constrained by both physics and causal information.

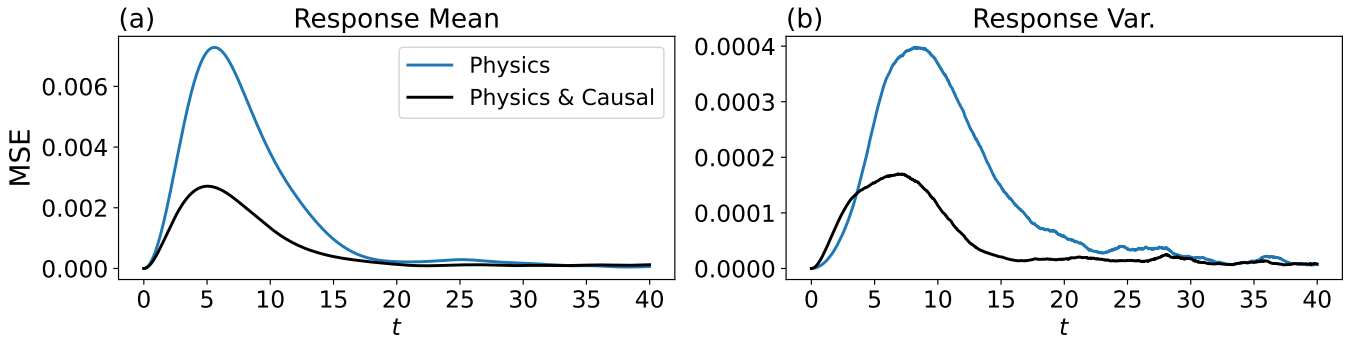


FIG. 9: Perturbed statistics in the linear regime. Panel (a): Total MSE over time for the mean response, computed from the full response operator $\mathbf{R}_t \in \mathbb{R}^{6,6}$ for each model. Panel (b): Same as Panel (a) but the response in ensemble variance.

IX. RESPONSE TO LARGE STEP FUNCTION FORCINGS IN THE CHARNEY-DEVORE MODEL

We now consider the nonlinear response regime by adding a step function forcing \mathbf{F} to both the numerical (CdV) and neural models. In the main text we focused on the case $\dot{\mathbf{x}} = \mathbf{F} + \mathbf{f}(\mathbf{x}) + \Sigma\xi(t)$, where $\mathbf{F} = (\sigma_1, 0, 0, 0, 0, 0)$ for $t \geq 0$, σ_1 being the std. dev. of the x_1 variable. We stress that this is a very large forcing, imposed on a model that had only access to unperturbed variability. Here, we perform six forcing experiments, applying a step forcing to each degree of freedom in turn with amplitude equal to its standard deviation: $\mathbf{F} = (\sigma_1, 0, \dots, 0), (0, \sigma_2, 0, \dots, 0), \dots, (0, \dots, 0, \sigma_6)$. For each case, we analyze the time-dependent response of the ensemble mean and variance of the full system. Results are shown in Fig. 10 (mean) and Fig. 11 (variance). The emulator constrained by both physics and causality generally leads to a better representation of the responses. This is clearly shown in the total MSE in Figure 12, aggregated over all response and perturbations (12), where the “physics and causal” emulator shows lower error in the long time response.

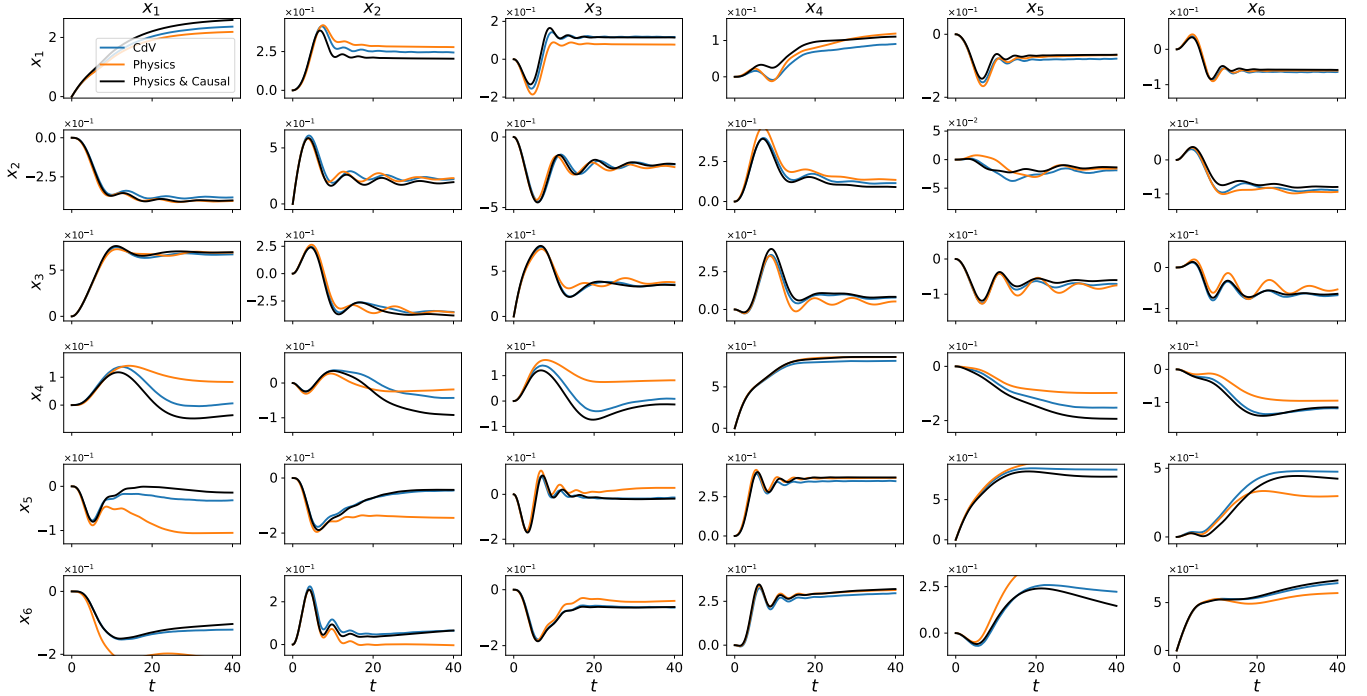


FIG. 10: Perturbed statistics in the nonlinear regime. Row (i) shows the response in ensemble mean to a step function forcing applied on x_i ; e.g. Row (1): response in ensemble mean response a step function forcing $\mathbf{F} = (\sigma_1, 0, 0, 0, 0, 0)$ applied for $t \geq 0$, where σ_1 is the standard deviation of x_1 . Row (2): same as Row (1) but using $\mathbf{F} = (0, \sigma_2, 0, 0, 0, 0)$. Labels: “CdV” refers to the numerical model; “Physics” is the model with only physics constrained; “Physics & Causal” is the model constrained by both physics and causal information.

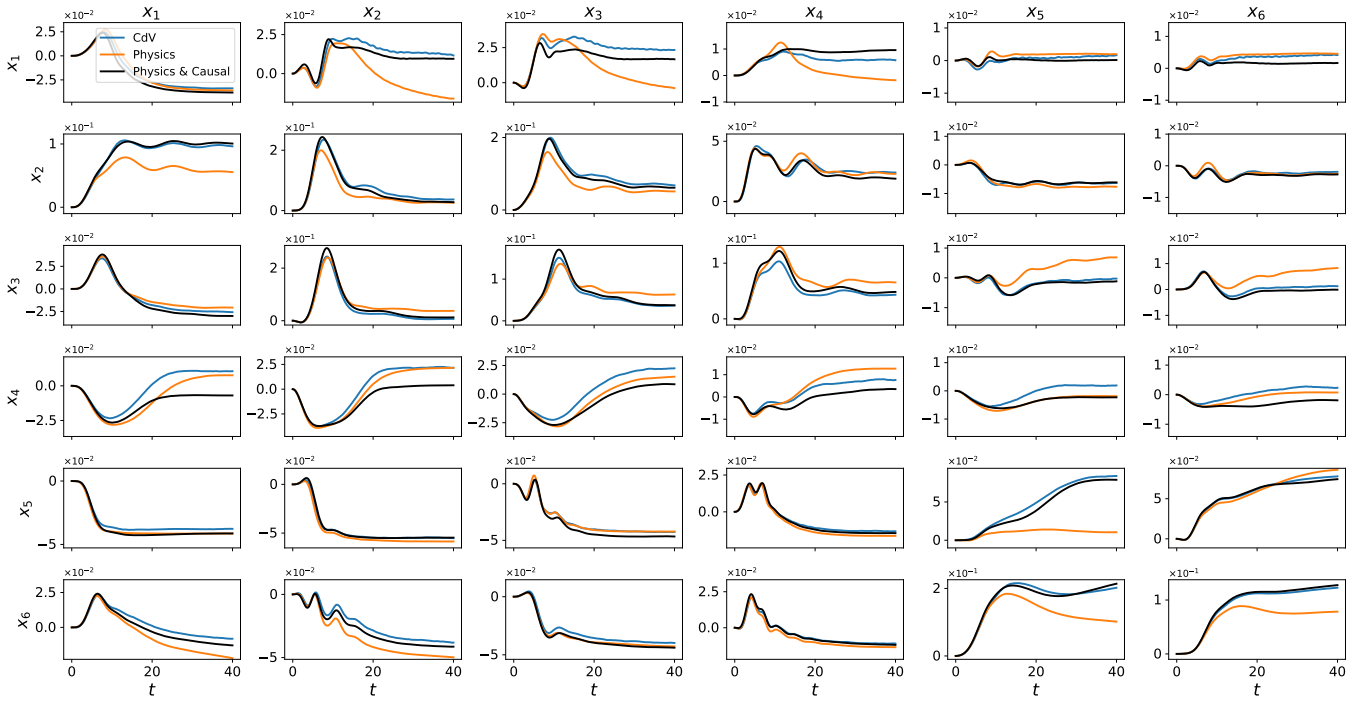


FIG. 11: Perturbed statistics in the nonlinear regime. Row (i) shows the response in ensemble variance to a step function forcing applied on x_i ; e.g. Row (1): response in ensemble mean to a step function forcing $\mathbf{F} = (\sigma_1, 0, 0, 0, 0, 0)$ applied for $t \geq 0$, where σ_1 is the standard deviation of x_1 . Row (2): same as Row (1) but using $\mathbf{F} = (0, \sigma_2, 0, 0, 0, 0)$. Responses are computed using an ensemble of $N_e = 10^5$ members. Labels: “CdV” refers to the numerical model; “Physics” is the model with only physics constrained; “Physics & Causal” is the model constrained by both physics and causal information.

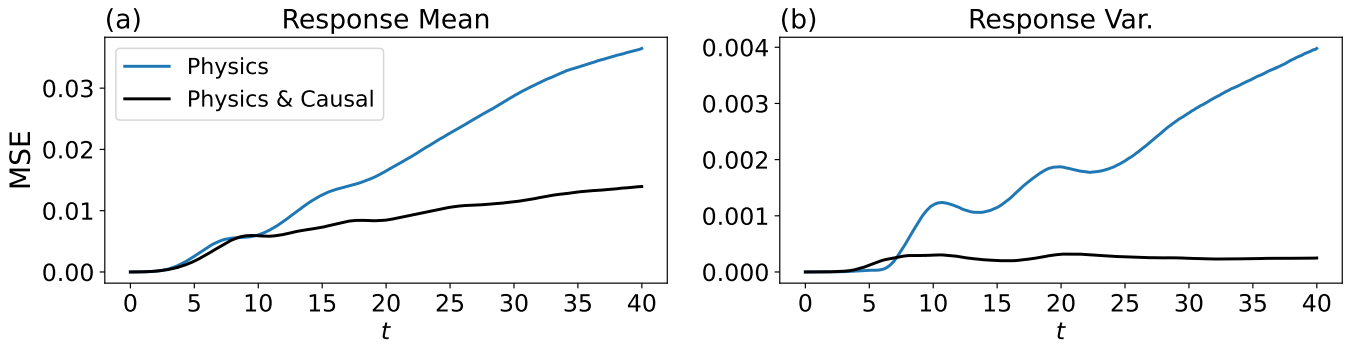


FIG. 12: Perturbed statistics in the nonlinear regime. Panel (a): Total MSE over time for the ensemble mean response. Panel (b): Same as Panel (a) but the response in ensemble variance.

X. SYMMETRY-BROKEN LORENZ-96 (L96) SYSTEM

a. Random forcing F_j . In this work, we introduce a time-independent forcing in the L96 system defined as $F_j = F + \eta_j$, where $\eta_j \sim \mathcal{N}(0, \sigma_F^2)$ with $\sigma_F = 10$. Due to the random component, we report the specific realization used in our experiments for reproducibility: $F_j = (6.1087865, 12.32213349, 28.87925261, 17.93974419, 25.202309, 21.77103791, 9.63536354, 21.4195222, 12.83404549, 12.77610884, 16.97167319, 4., 27.92166104, 9.28910325, 26.0026942, 17.36321124, 31.3203308, 9.40030586, 12.88205144, 19.37769127)$.

A. Stationary statistics

The marginals of the invariant distribution of the L96 system predicted by the two emulators are shown in Fig. 13. The corresponding autocorrelation functions are reported in Fig. 14.

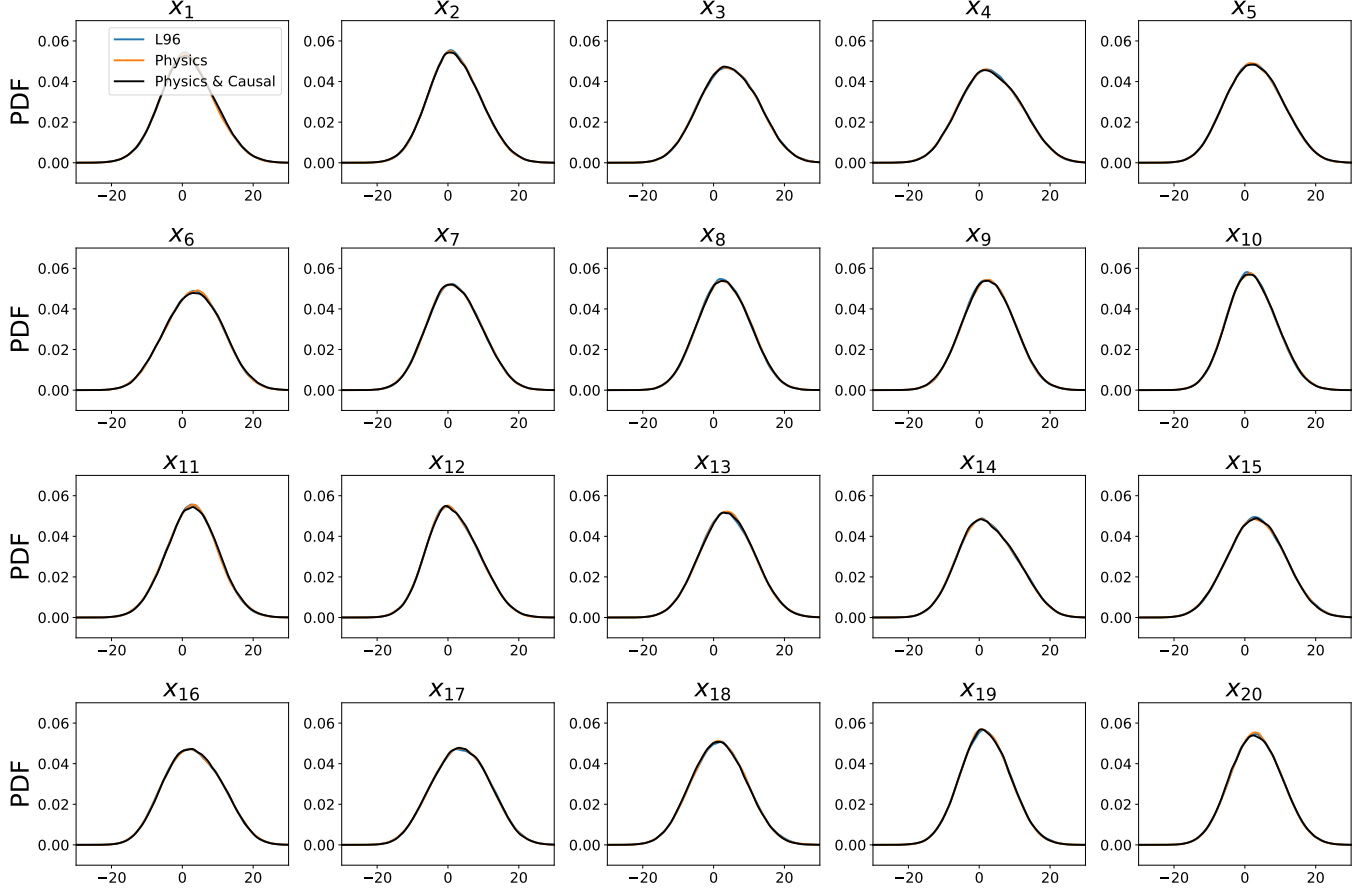


FIG. 13: Stationary statistics. Stationary distributions (PDFs) of the variables x_1, \dots, x_{20} of the L96 system considered in the main text. Labels: “L96” refers to the numerical model; “Physics” is the model with only physics constrained; “Physics & Causal” is the model constrained by both physics and causal information.

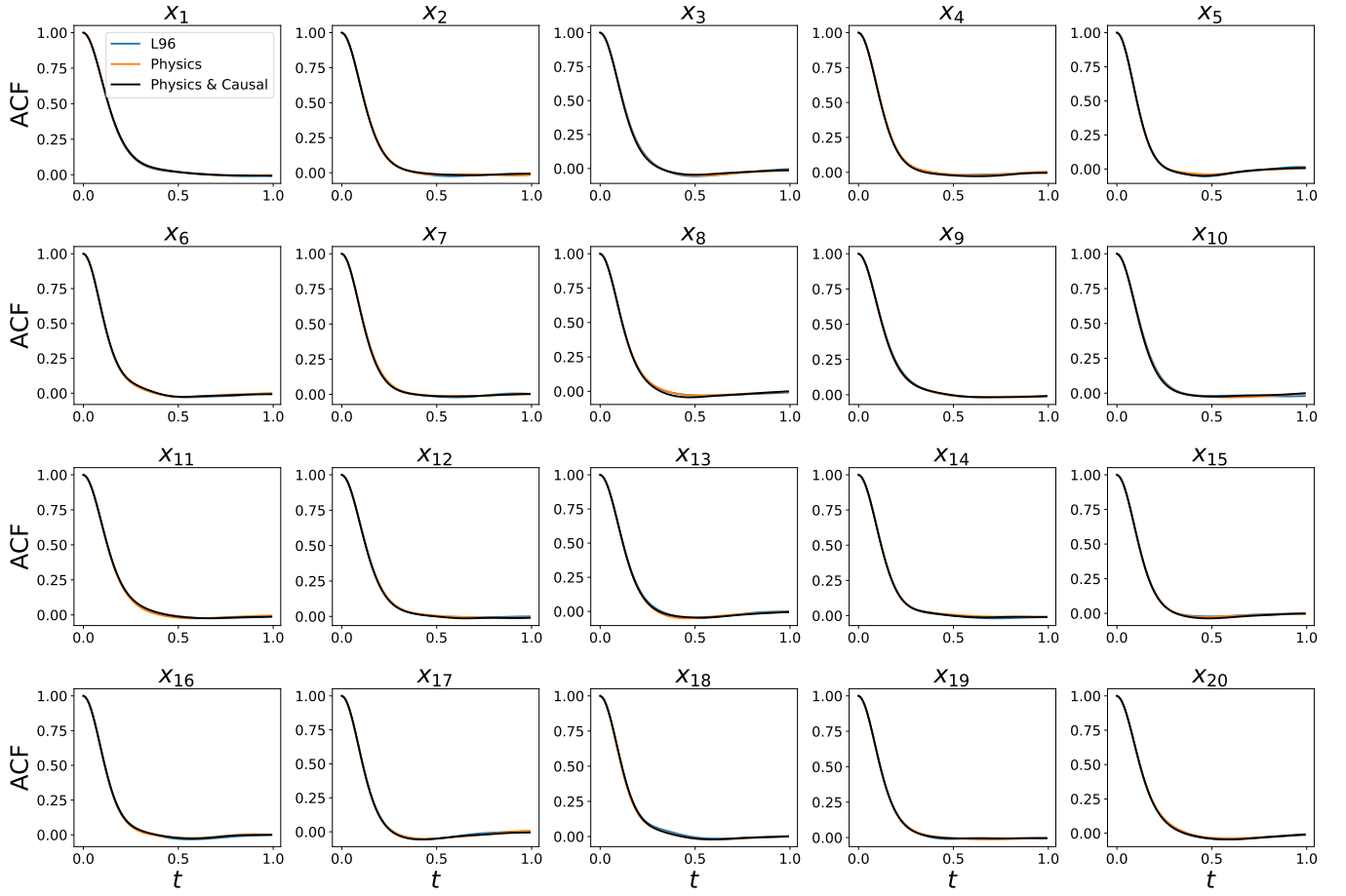


FIG. 14: Autocorrelation functions (ACFs) of the variables x_1, \dots, x_{20} of the L96 system considered in the main text. Labels: “L96” refers to the numerical model; “Physics” is the model with only physics constrained; “Physics & Causal” is the model constrained by both physics and causal information.